

## MODELING THE INFRARED EMISSION FROM THE HD 141569A DISK

AIGEN LI AND J. I. LUNINE

Theoretical Astrophysics Program, Lunar and Planetary Laboratory,  
and Steward Observatory, University of Arizona, Tucson, AZ 85721;  
agli@lpl.arizona.edu, jlunine@lpl.arizona.edu

Received 2003 April 2; accepted 2003 May 16

### ABSTRACT

We model the infrared (IR) emission from the double-ring disk of HD 141569A, using a porous dust model that was previously shown to be successful in reproducing the spectral energy distributions (SEDs) of the disks around  $\beta$  Pictoris and HR 4796A. The dust consists of either unaltered or highly processed interstellar materials and vacuum with a volume fraction of  $\sim 90\%$ . Together with a population of polycyclic aromatic hydrocarbon (PAH) molecules, of which a large fraction are charged, the porous dust model made of coagulated but otherwise unaltered protostellar interstellar grains provides an excellent fit to the entire SED from the mid-IR to millimeter wavelengths, including the PAH mid-IR emission features. The nondetection of the  $21\ \mu\text{m}$  crystalline silicate feature predicted from the porous dust model composed of highly processed grains (mainly crystalline silicate dust) imposes an upper limit of  $\sim 10\%$  on the mass fraction of crystalline silicates. Spectroscopic and broadband photometric predictions are made for *SIRTf* observations, which will provide further tests of the applicability of the porous dust model to circumstellar disks.

*Subject headings:* circumstellar matter — dust, extinction — infrared: stars —  
planetary systems: protoplanetary disks — stars: individual (HD 141569A)

### 1. INTRODUCTION

Since dust disks around young stars, depending on their age, are the source material or the remnants of newly formed planets, the physical, chemical, and dynamical properties of circumstellar disks and their constituent grains are crucial in understanding the formation process of planetary systems.

Over the past two decades, impressive evidence has been assembled for the commonality of circumstellar dust disks around pre-main-sequence stars (T Tauri and Herbig Ae/Be stars), main-sequence (MS) stars, post-MS stars (red giants), and a white dwarf (for reviews, see Backman & Paresce 1993; Habing et al. 2001; Zuckerman 2001; Lagrange, Backman, & Artymowicz 2000). To date, at least 15% of the A- to K-type stars are found to have dust disks around them (see Lagrange et al. 2000). The majority of these disks are spatially extensive, with their dust quantities and intensities of scattered starlight and dust thermal emission gradually decreasing outward from the central stars. However, so far there exist four exceptions: (1)  $\epsilon$  Eridani—a  $\sim 800$  Myr old (Henry et al. 1996) K2V MS star—has a nearly face-on dust ring with mass and radius ( $r \sim 60$  AU) similar to the solar system Kuiper Belt and is thought to be an analog to the young solar system (Greaves et al. 1998); (2) Fomalhaut ( $\alpha$  PsA)—a  $\sim 200$  Myr old (Barrado y Navascués et al. 1997) A3V MS star—exhibiting a “doughnut-like” dust annulus with a radial distance of  $\sim 150$  AU from the star and a width of  $\sim 60$  AU (Holland et al. 1998, 2003); (3) HR 4796A—a  $\sim 8 \pm 3$  Myr old A0V star (see Jura et al. 1998)—displaying a ringlike disk peaking at  $\sim 70$  AU from the central star and abruptly truncated both inward and outward with a width of  $\lesssim 17$  AU (Schneider et al. 1999; Koerner et al. 1998; Jayawardhana et al. 1998; Telesco et al. 2000); and (4) HD 141569A—a nearby (distance to the Earth  $d \approx 99$  pc; van den Ancker, de Winter, & Tjin A Djie 1998),  $\sim 5 \pm 3$  Myr old (Weinberger et al. 2000) pre-MS Herbig Ae/Be star—with a spectral type of B9.5 V, an effec-

tive temperature of  $T_{\text{eff}} \approx 10,000$  K, and a surface gravity of  $\lg g \approx 4.0$  (Dunkin, Barlow, & Ryan 1997).

The presence of dust around HD 141569A was first reported by Jaschek, Jaschek, & Egret (1986), de Grijp, Miley, & Lub (1987), and Walker & Wolstencroft (1988) based on the *Infrared Astronomical Satellite (IRAS)* detection of infrared (IR) excess greater than expected from its photosphere. It has recently been imaged in scattered light and thermal IR emission. With the discovery of its large and morphologically complicated debris disk (see below), HD 141569A has recently aroused considerable interest.

The disk around HD 141569A appears to have two ring-like structures: an outer ring at  $\sim 325$  AU from the star with a width of  $\sim 150$  AU and an inner ring at  $\sim 185$  AU. The outer ring was reported independently by Augereau et al. (1999a) and Weinberger et al. (1999) based on the 1.6 and 1.1  $\mu\text{m}$  imaging, respectively, of the scattered light. They both used the Near-Infrared Camera and Multi-Object Spectrometer (NICMOS) on the *Hubble Space Telescope (HST)*. The inner ring was discovered by Weinberger et al. (1999) at 1.1  $\mu\text{m}$  using the same instrument. Weinberger et al. (1999) also reported the detection of a gap, or “dip,” (a region of depleted material) at  $\sim 250$  AU from the star with a width of  $\sim 60$  AU. They interpreted the gap as a sign of one or more planets orbiting within the disk (the planets do not have to be in the gap), but other explanations, such as dust migration, also exist (see, e.g., Takeuchi & Artymowicz 2001).

This ring-gap-ring structure was later confirmed by optical coronagraphic observations made by Mouillet et al. (2001) at an effective wavelength of 5850 Å using the *HST* Space Telescope Imaging Spectrograph. With a higher spatial resolution and a higher signal-to-noise ratio than the *HST* NICMOS data, Mouillet et al. (2001) found that the inner ring, with an FWHM of  $\sim 50$  AU, actually peaks at  $\sim 200 \pm 5$  AU. Strong brightness asymmetry was also reported by Mouillet et al. (2001). This asymmetry, interpreted as a result of the gravitational perturbation caused

by putative massive planets within the disk by the two stellar companions HD 141569B and HD 141569C, or both types of objects (Mouillet et al. 2001), was confirmed by the ground-based 2.2  $\mu\text{m}$  near-IR imaging observation at the Palomar 200 inch (5.08 m) telescope using the adaptive optics system (Boccaletti et al. 2003).

In addition to the two annuli, the existence of a third dust component—a population of warm, mid-IR-emitting dust within  $\sim 100$  AU from the star—was recently reported by Fisher et al. (2000). It was shown that the 10.8 and 18.2  $\mu\text{m}$  emission observed with the University of Florida Observatory Spectrometer and Camera for the Infrared (OSCIR) on the Keck II Telescope extend out to  $\sim 100$  AU from the star (Fisher et al. 2000). The existence of such an extended, warm source close to the star, originally suggested by Augereau et al. (1999a) to account for the disk IR emission at wavelengths  $\lambda \lesssim 10 \mu\text{m}$ , was later confirmed by the 12.5, 17.9, and 20.8  $\mu\text{m}$  imaging using the JPL Mid-InfraRed Large-well Imager (MIRLIN) on the Keck II Telescope (Marsh et al. 2002).

More recently, the high-resolution channel coronagraphic  $B$ ,  $V$ , and  $I$  images of the HD 141569A disk obtained with the *HST* Advanced Camera for Surveys revealed a tightly wound spiral structure with two arms, one of which stretches outward to reach the nearby companion stars (Clampin et al. 2003).

In a previous paper (Li & Lunine 2003), we have shown that the IR emission from the HR 4796A disk can be well fitted by a model invoking highly porous cometary-type dust. The porous cometary dust model was originally proposed for the  $\beta$  Pictoris disk and was shown to be successful in reproducing its spectral energy distribution (SED) from the near-IR to millimeter wavelengths, including the 10  $\mu\text{m}$  amorphous and the 11.3  $\mu\text{m}$  crystalline silicate features (Li & Greenberg 1998). In this paper we model the observed IR and millimeter photometric and mid-IR spectroscopic signatures of HD 141569A. The objectives of this paper are threefold: (1) We wish to infer the physical and chemical properties of the dust in the HD 141569A disk and its relationship to the formation of planets. (2) We wish to know how widely applicable the porous dust model is; if it can be shown that the porous dust model is also valid for many other disks at different evolutionary stages and with different geometrical structures, it will be a valuable guide for interpreting future data sets. This is of particular importance given that the upcoming *Space Infrared Telescope Facility* (*SIRTF*) will accumulate a rich set of IR photometric and spectroscopic data for a large number of dust disks; we would hope that the porous dust model presented in this and related papers could serve as a starting point in analyzing these data. (3) We wish to make near- and mid-IR spectral and broadband photometry predictions for the HD 141569A disk; these predictions can be compared to future *SIRTF* observations in order to test further the validity of the porous dust model.

This paper is organized as follows: We first summarize in § 2 the photometric and spectroscopic data available for the HD 141569A disk that are relevant in modeling the IR emission of the disk. We then give an overview discussion in § 3.1 of the proposed dust model, with emphasis on dust composition and morphology from the point of view of protoplanetary disk evolution, followed by detailed discussions of the polycyclic aromatic hydrocarbon (PAH) component in § 3.1.1 and the porous dust component in § 3.1.2. The IR

emission modeling technique is presented in § 3.1.3. In § 3.1.4 the PAH photoelectric emission rates and the electron recombination rates are calculated, using the methods described in Appendices A and B. The key model parameters are discussed and specified in § 3.1.5. Model results are presented in § 3.2. In § 4 we discuss (1) previous studies of the SED modeling of the HD 141569A disk, (2) comparison of the HD 141569A disk with the HR 4796A disk, (3) exploration of parameter space (§ 4.1), (4) PAH photo-destruction (§ 4.2), and (5) dust loss through radiation expulsion and Poynting-Robertson drag (§ 4.3). In § 4.4 we calculate the dust IR flux densities integrated over the *SIRTF* Infrared Array Camera (IRAC) and Multiband Imaging Photometer (MIPS) bands predicted for our best-fitting models. Spectroscopic predictions are also made for the *SIRTF* Infrared Spectrograph (IRS) observations. The major conclusions are summarized in § 5.

## 2. AVAILABLE PHOTOMETRIC AND SPECTROSCOPIC DATA

To facilitate modeling of the dust properties of the HD 141569A disk, we have assembled the available optical, IR, and millimeter photometric data and mid-IR spectra. These include (1) the  $BV$  optical photometry (Sylvester et al. 1996); (2) the  $JHKLL'M$  near-IR photometry obtained by Sylvester et al. (1996) using the single-channel bolometer UKT9 at the United Kingdom Infrared Telescope (UKIRT); (3) the 12, 25, 60, and 100  $\mu\text{m}$  *IRAS* photometry (Sylvester et al. 1996); (4) the 10.8 and 18.2  $\mu\text{m}$  Keck II OSCIR imaging by Fisher et al. (2000); (5) the 12.5, 17.9, and 20.8  $\mu\text{m}$  Keck II MIRLIN imaging by Marsh et al. (2002); (6) the 7.5–13.5  $\mu\text{m}$  (spectral resolution  $\Delta\lambda = 0.17 \mu\text{m}$ ) and 15.8–23.9  $\mu\text{m}$  ( $\Delta\lambda = 0.27 \mu\text{m}$ ) spectroscopy obtained by Sylvester et al. (1996) using the UKIRT Cooled Grating Spectrometer 3 (CGS3); and (7) the 1350  $\mu\text{m}$  Submillimeter Common-User Bolometer Array (SCUBA) measurement by Sylvester, Dunkin, & Barlow (2001) using the James Clerk Maxwell Telescope (JCMT). Taking  $E(B-V) = 0.095$  (Weinberger et al. 1999), we have corrected the interstellar reddening assuming an  $R_V = 3.1$  (total-to-selective extinction) interstellar extinction law (see Table 6 in Li & Draine 2001b).

Table 1 summarizes the photometric data listed above, the instruments/telescopes and their beam sizes through which the observational data were obtained, and the stellar atmospheric and dust disk contributions to each photometric band. In Figure 1a we plot the reddening-corrected optical, IR, and millimeter photometric results as well as the  $T_{\text{eff}} = 10,000$  K and  $\lg g = 4.0$  Kurucz model atmospheric spectrum. Figure 1b illustrates the CGS3 mid-IR spectrum, which clearly exhibits the 11.3  $\mu\text{m}$  out-of-plane C-H bending feature and the long-wavelength wing of the 7.7  $\mu\text{m}$  C-C stretching feature (see Li & Draine 2001b for the PAH band assignment). For the sake of comparison, the 10.8 and 18.2  $\mu\text{m}$  Keck II OSCIR data, the 12 and 25  $\mu\text{m}$  *IRAS* data, and the 12.5, 17.9, and 20.8  $\mu\text{m}$  Keck II MIRLIN data are also plotted in Figure 1b. It is seen that these mid-IR data closely agree with one another.<sup>1</sup> The largest discrepancy

<sup>1</sup> The 12  $\mu\text{m}$  *IRAS* data are about 12% higher than the band-averaged CGS3 spectrum. We have therefore reduced the former by a factor of 1.12 to bring the 12  $\mu\text{m}$  *IRAS* data into agreement with the CGS3 spectrum.

TABLE 1  
EXISTING OPTICAL, IR, AND MILLIMETER PHOTOMETRIC DATA FOR THE HD 141569A SYSTEM

$\lambda$ ( $\mu\text{m}$ )	$F_{\nu}^{\text{obs a,b}}$ (Jy)	$F_{\nu}^{\text{star c}}$ (Jy)	$F_{\nu}^{\text{dust d}}$ (Jy)	$F_{\lambda}^{\text{obs a}}$ ( $\text{ergs s}^{-1} \text{cm}^{-2} \mu\text{m}^{-1}$ )	$F_{\lambda}^{\text{star c}}$ ( $\text{ergs s}^{-1} \text{cm}^{-2} \mu\text{m}^{-1}$ )	$F_{\lambda}^{\text{dust d}}$ ( $\text{ergs s}^{-1} \text{cm}^{-2} \mu\text{m}^{-1}$ )	Telescope/Instrument	Beam/Aperture Size	Reference
0.45 (B)	10.50	10.50	...	$1.56 \times 10^{-7}$	$1.56 \times 10^{-7}$	...	...	...	1
0.55 (V)	6.70	6.70	...	$6.64 \times 10^{-8}$	$6.64 \times 10^{-8}$	...	...	...	1
1.22 (J)	3.19	3.19	...	$6.43 \times 10^{-9}$	$6.43 \times 10^{-9}$	...	UKIRT	7"8	1
1.65 (H)	2.02	2.02	...	$2.23 \times 10^{-9}$	$2.23 \times 10^{-9}$	...	UKIRT	7"8	1
2.18 (K)	1.29	1.29	...	$8.14 \times 10^{-10}$	$8.14 \times 10^{-10}$	...	UKIRT	7"8	1
3.55 (L)	0.59	0.58	0.018	$1.41 \times 10^{-10}$	$1.37 \times 10^{-10}$	$4.29 \times 10^{-12}$	UKIRT	7"8	1
3.76 (L')	0.54	0.50	0.040	$1.14 \times 10^{-10}$	$1.06 \times 10^{-10}$	$8.54 \times 10^{-12}$	UKIRT	7"8	1
4.77 (M)	0.40	0.33	0.070	$5.33 \times 10^{-11}$	$4.41 \times 10^{-11}$	$9.25 \times 10^{-12}$	UKIRT	5"0	1
12.....	0.49	0.058	0.43	$1.02 \times 10^{-11}$	$1.21 \times 10^{-12}$	$9.02 \times 10^{-12}$	IRAS	1'	1
25.....	1.87	0.014	1.86	$8.98 \times 10^{-12}$	$6.64 \times 10^{-14}$	$8.91 \times 10^{-12}$	IRAS	1'	1
60.....	5.54	0.0024	5.54	$4.62 \times 10^{-12}$	$2.04 \times 10^{-15}$	$4.61 \times 10^{-12}$	IRAS	1'	1
100.....	3.48	0.0009	3.48	$1.04 \times 10^{-12}$	$2.65 \times 10^{-16}$	$1.04 \times 10^{-12}$	IRAS	1'	1
10.8.....	$0.318 \pm 0.016$	0.071	0.25	$8.18 \times 10^{-12}$	$1.83 \times 10^{-12}$	$6.34 \times 10^{-12}$	Keck II OSCIR	7"9 $\times$ 7"9	2
18.2.....	$0.646 \pm 0.035$	0.026	0.62	$5.85 \times 10^{-12}$	$2.34 \times 10^{-13}$	$5.62 \times 10^{-12}$	Keck II OSCIR	7"9 $\times$ 7"9	2
12.5 <sup>e</sup> .....	$0.333 \pm 0.022$	0.054	0.28	$6.39 \times 10^{-12}$	$1.03 \times 10^{-12}$	$5.36 \times 10^{-12}$	MIRLIN/Keck II	5"	3
17.9 <sup>e</sup> .....	$0.936 \pm 0.094$	0.027	0.91	$8.76 \times 10^{-12}$	$2.50 \times 10^{-13}$	$8.51 \times 10^{-12}$	MIRLIN/Keck II	5"	3
20.8 <sup>e</sup> .....	$1.19 \pm 0.16$	0.020	1.17	$8.25 \times 10^{-12}$	$1.38 \times 10^{-13}$	$8.11 \times 10^{-12}$	MIRLIN/Keck II	5"	3
1350.....	$0.0054 \pm 0.001$	0	0.0054	$8.89 \times 10^{-18}$	$8.03 \times 10^{-21}$	$8.88 \times 10^{-18}$	SCUBA	22"	4

NOTE.—See § 2. In the SED modeling presented in later sections, we include both the CGS3 mid-IR spectrum and the IRAS, Keck II OSCIR, and SCUBA photometry.

<sup>a</sup> Total flux density observed from the Earth.

<sup>b</sup>  $F_{\nu}/Jy \equiv (F_{\lambda}/\text{ergs s}^{-1} \text{cm}^{-2} \mu\text{m}^{-1})(\lambda/\mu\text{m})^2 (10^9/3)$ .

<sup>c</sup> Stellar photospheric contribution to the observed flux density.

<sup>d</sup> Dust IR excess from the disk.

<sup>e</sup> The Keck II MIRLIN instrument has a field of view of  $18'' \times 18''$ . But the flux given in this table was obtained by an integration over a  $5''$  diameter circular aperture (see Marsh et al. 2002).

REFERENCES.—(1) Sylvestre et al. 1996. (2) Fisher et al. 2000. (3) Marsh et al. 2002. (4) Sylvestre et al. 2001.

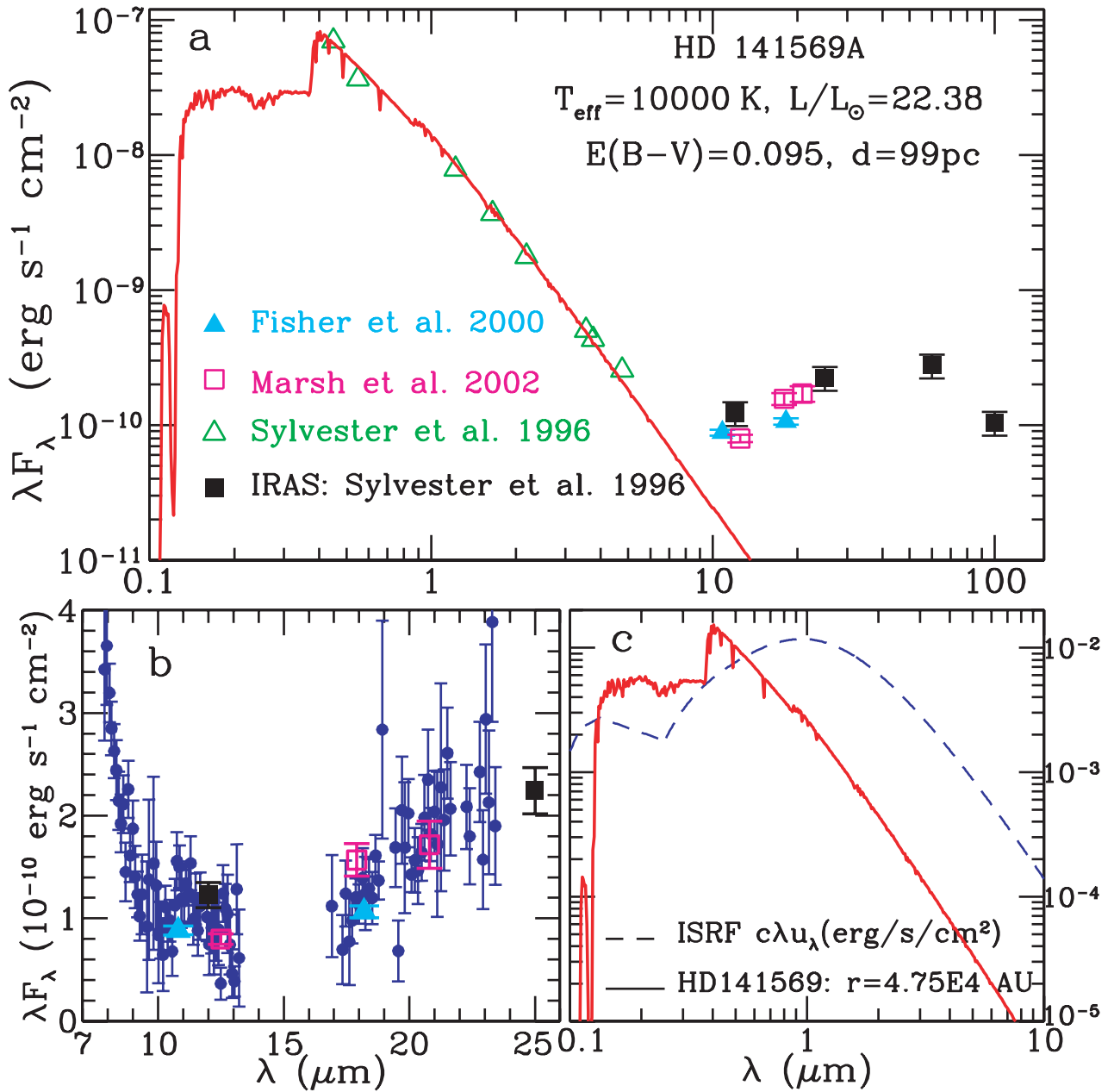


FIG. 1.—(a) SED of the HD 141569A system (see § 2 and Table 1). *Red solid line*: The  $T_{\text{eff}} = 10,000$  K and  $\lg g = 4.0$  Kurucz model atmospheric spectrum. *Green open triangles*: Optical and near-IR photometry (Sylvester et al. 1996). *Cyan filled triangles*: The 10.8 and 18.2  $\mu\text{m}$  Keck II OSCIR photometry (Fisher et al. 2000). *Black filled squares*: The 12, 25, 60, and 100  $\mu\text{m}$  IRAS photometry (Sylvester et al. 1996). *Magenta open squares*: The 12.5, 17.9, and 20.8  $\mu\text{m}$  Keck II MIRLIN photometry (Marsh et al. 2002). (b) CGS3 mid-IR spectrum (*blue filled circles*; Sylvester et al. 1996) as well as the OSCIR, MIRLIN, and IRAS photometry. All observational data in (a) and (b) have been dereddened, but the stellar photospheric contributions to the IR photometric and spectroscopic bands have not been subtracted. (c) The HD 141569A radiation field at a distance of  $r = 4.75 \times 10^4$  AU from the star (*red solid line*), which equals the 912  $\text{\AA}$ -1  $\mu\text{m}$  general interstellar radiation field (*blue dashed line*; MMP; see § 3.1.1).

( $\approx 30\%$ ) occurs for the 17.9  $\mu\text{m}$  Keck II MIRLIN data (Marsh et al. 2002) and the 18.2  $\mu\text{m}$  Keck II OSCIR data (Fisher et al. 2000). This discrepancy cannot be explained in terms of the difference in the aperture sizes of these two instruments. As a matter of fact, the former (which has a higher 17.9  $\mu\text{m}$  flux density) were obtained using a smaller aperture. The CGS3 mid-IR spectrum, obtained with a  $5'' \times 5''$  beam, appears to be intermediate between the MIRLIN and the OSCIR data. Therefore, we ascribe this discrepancy to observational uncertainties. Both data points are included in our detailed dust modeling.

### 3. MODELING THE DUST IR EMISSION

#### 3.1. Dust Model

Interstellar grains undergo coagulative growth in cold, dense, molecular clouds and protostellar and protoplanetary dust disks. This process creates dust with fluffy, inhomogeneous structures and fairly quickly leads to the formation of planetesimals of cometary to asteroidal sizes.

Based on its short lifetime due to radiative expulsion, the dust in the HD 141569A disk is thought to be of secondary debris origin (Weinberger et al. 1999, 2000; Fisher et al.

2000; Marsh et al. 2002); i.e., the dust is generated by the breaking down of large bodies, like planetesimals, comets, and asteroids, rather than a direct remnant left over from the star formation process. Since planetesimals and comets are formed through coagulation of porous dust aggregates (Cameron 1975, 1995; Weidenschilling & Cuzzi 1993; Greenberg & Li 1999; Beckwith, Henning, & Nakagawa 2000), the dust generated by collisions of planetesimals should resemble the original dust from which they are built up.

Following Li & Lunine (2003), we model the HD 141569A dust as porous aggregates of either processed or unprocessed interstellar materials. We consider two dust types—each represents an extreme case—the “cold-coagulation” dust model and the “hot-nebula” dust model. While the former assumes that the dust aggregate is formed through cold coagulation of unaltered protostellar interstellar grains, the latter goes to the other extreme by assuming that the constituent grains in the dust aggregate are highly processed in the protostellar nebula, where the originally amorphous silicate grains all are annealed and the carbon grains all are destroyed by oxidation and converted into CO (see Li & Lunine 2003 for details).

A porous dust grain is characterized by (1) its fluffiness or porosity  $P$  (the fractional volume of vacuum); (2) its spherical radius  $a$  (the radius of the sphere encompassing the entire aggregate; we assume that all grains are spherical in shape); and (3) composition—the cold-coagulation dust model assumes the dust to be composed of amorphous silicate and carbonaceous materials (and H<sub>2</sub>O-dominated ices in regions colder than  $\sim 110$ – $120$  K), and the hot-nebula dust model assumes the dust to be composed of only crystalline silicates (and ices in cold regions). As discussed in Li & Lunine (2003), for the cold-coagulation dust model, the mixing mass ratios for the silicate, carbon, and ice constituent grains are approximately derived, by assuming cosmic abundance, to be  $m_{\text{carb}}/m_{\text{sil}} \approx 0.7$  and  $m_{\text{ice}}/(m_{\text{sil}} + m_{\text{carb}}) \approx 0.8$ , where  $m_{\text{sil}}$ ,  $m_{\text{carb}}$ , and  $m_{\text{ice}}$  are, respectively, the total mass of the silicate, carbon, and ice subgrains. For the hot-nebula dust model, we take  $m_{\text{carb}}/m_{\text{sil}} = 0$  and  $m_{\text{ice}}/m_{\text{sil}} = \frac{1}{3}$  (see Li & Lunine 2003). We adopt a mass density of  $\rho_{\text{sil}} = 3.5 \text{ g cm}^{-3}$ ,  $\rho_{\text{carb}} = 1.8 \text{ g cm}^{-3}$ , and  $\rho_{\text{ice}} = 1.2 \text{ g cm}^{-3}$ , respectively, for the silicate, carbonaceous, and ice materials.<sup>2</sup>

In addition to the porous dust component discussed above, the presence of PAH molecules in the HD 141569A disk is clearly indicated by the red wing of the  $7.7 \mu\text{m}$  feature and the  $11.3 \mu\text{m}$  feature seen in the CGS3 mid-IR spectrum (Sylvester et al. 1996; see Fig. 1b). Therefore, we consider two dust populations in our models: the porous dust component (§ 3.1.1) and the PAH component (§ 3.1.2).

### 3.1.1. Polycyclic Aromatic Hydrocarbon Dust

PAHs are excited by ultraviolet (UV), visible, and, to a lesser extent, long-wavelength photons (Li & Draine 2002a). Following Li & Draine (2002a), we define  $U(r)$  as the  $912 \text{ \AA}$ – $1 \mu\text{m}$  starlight intensity incident on the HD 141569A disk at a distance  $r$  from the central star relative to the value for the Mathis, Mezger, & Panagia (1983, here-

<sup>2</sup> For pure H<sub>2</sub>O ice, we have  $\rho_{\text{ice}} \approx 1.0 \text{ g cm}^{-3}$ . Since interstellar ice is a “dirty” mixture of H<sub>2</sub>O, NH<sub>3</sub>, CO, CO<sub>2</sub>, CH<sub>3</sub>OH, CH<sub>4</sub>, and many other molecules (see Appendix A in Li & Lunine 2003), we adopt  $\rho_{\text{ice}} = 1.2 \text{ g cm}^{-3}$  for “dirty ice” material (Greenberg 1968).

after MMP) solar neighborhood interstellar radiation field<sup>3</sup>:

$$U(r) \equiv \frac{(R_*/2r)^2 \int_{912\text{\AA}}^{1\mu\text{m}} F_\lambda^* d\lambda}{\int_{912\text{\AA}}^{1\mu\text{m}} c u_\lambda^{\text{ISRF}} d\lambda} \approx \left( \frac{4.75 \times 10^4 \text{ AU}}{r} \right)^2, \quad (1)$$

where  $R_*$  ( $\approx 7.32 \times 10^{-3} \text{ AU}$ ) is the HD 141569A stellar radius,  $F_\lambda^*$  is the flux per unit wavelength (in units of  $\text{ergs s}^{-1} \text{ cm}^{-2} \mu\text{m}^{-1}$ ) at the top of the illuminating star’s atmosphere, which is approximated by the Kurucz model atmospheric spectrum for B9.5 V stars ( $T_{\text{eff}} = 10,000 \text{ K}$  and  $\lg g = 4.0$ ; Kurucz 1979),  $c$  is the speed of light, and  $u_\lambda^{\text{ISRF}}$  is the energy density of the MMP interstellar radiation field. In Figure 1c we plot the starlight spectrum at  $r = 4.75 \times 10^4 \text{ AU}$ , which corresponds to  $U = 1$ . Since the HD 141569A disk extends to a distance of only  $\sim 500 \text{ AU}$ , the dust in this disk receives far more *intense* irradiation than the dust in the diffuse interstellar medium:  $U > 9000!$

Illuminated by starlight with an intensity of  $U$ , the IR emissivity per *gram* of dust (in units of  $\text{ergs s}^{-1} \mu\text{m}^{-1} \text{ g}^{-1}$ ) for a mixture of neutral and ionized PAHs with a size distribution of  $dn_{\text{PAH}}/da$  is

$$\begin{aligned} J_\lambda^{\text{PAH}}(U) = & \int_{a_{\text{min}}^{\text{PAH}}}^{\infty} da \frac{dn_{\text{PAH}}}{da} \int_0^\infty dT 4\pi B_\lambda(T) \\ & \times \left\{ \phi_{\text{ion}}(U, a) C_{\text{abs}}^{\text{PAH}^+}(a, \lambda) \left( \frac{dP^{\text{PAH}^+}}{dT} \right) \right. \\ & \left. + [1 - \phi_{\text{ion}}(U, a)] C_{\text{abs}}^{\text{PAH}^0}(a, \lambda) \left( \frac{dP^{\text{PAH}^0}}{dT} \right) \right\} \\ & \times \left\{ \int_{a_{\text{min}}^{\text{PAH}}}^{\infty} da \frac{dn_{\text{PAH}}}{da} \frac{4\pi}{3} a^3 \rho_{\text{PAH}} \right\}^{-1}, \quad (2) \end{aligned}$$

where  $a$  is the spherical radius of a PAH molecule,<sup>4</sup>  $a_{\text{min}}^{\text{PAH}}$  is the lower-cutoff PAH size,  $C_{\text{abs}}^{\text{PAH}^0}$  and  $C_{\text{abs}}^{\text{PAH}^+}$  are the absorption cross sections for neutral and ionized PAH molecules, respectively (see Li & Draine 2001b),  $B_\lambda(T)$  is the Planck function at temperature  $T$ ,  $dP^{\text{PAH}^0}(U, a, T)$  and  $dP^{\text{PAH}^+}(U, a, T)$  are the probabilities that the vibrational temperature will be in  $[T, T + dT]$  for neutral and charged PAHs, respectively, illuminated by starlight intensity  $U$ ,  $\phi_{\text{ion}}(U, a)$  is the probability of finding a PAH molecule of radius  $a$  in a nonzero charge state, and  $\rho_{\text{PAH}}$  is the mass density of PAHs, which is taken to be that of graphite ( $\approx 2.24 \text{ g cm}^{-3}$ ).

Based on the “thermal discrete” method (Draine & Li 2001), the temperature distribution functions  $dP/d \ln T$  have been computed by Li & Draine (2002a) for neutral and charged PAHs and ultrasmall silicate grains of a range of sizes  $3.5 \text{ \AA} \lesssim a \lesssim 350 \text{ \AA}$  illuminated by stars with a range of effective temperatures  $3000 \text{ K} \lesssim T_{\text{eff}} \lesssim 30,000 \text{ K}$  and with a range of starlight intensities  $0.1 \lesssim U \lesssim 10^5$ . In this work we take the Li & Draine (2002a)  $dP/d \ln T$  results for  $T_{\text{eff}} = 10,000 \text{ K}$ .

<sup>3</sup> For radiation fields with the same  $912 \text{ \AA}$ – $1 \mu\text{m}$  intensity, the 6–13.6 eV starlight intensity of the  $T_{\text{eff}} = 10,000 \text{ K}$  Kurucz radiation field is about 1.27 times that of the MMP field.

<sup>4</sup> Small PAHs (with  $\lesssim 100$  carbon atoms) are expected to be planar (see Appendix A in Draine & Li 2001). The term “PAH radius” used in this paper refers to the radius  $a$  of a spherical grain with the same carbon density as graphite ( $2.24 \text{ g cm}^{-3}$ ) and containing the same number of carbon atoms  $N_C$ :  $a \equiv 1.288 N_C^{1/3} \text{ \AA}$  [or  $N_C \equiv 0.468 (a/\text{\AA})^3$ ].

We adopt a lognormal size distribution for the PAHs in the HD 141569A disk, characterized by two parameters:  $a_0$  and  $\sigma$ ;  $a_0$  and  $\sigma$  determine, respectively, the peak location and the width of the lognormal distribution:

$$\frac{dn_{\text{PAH}}}{da} = \frac{1}{\sqrt{\pi/2}\sigma \{1 - \text{erf}[\ln(a/a_0)/\sqrt{2}\sigma]\}} \times \frac{1}{a} \exp\left\{-\frac{1}{2}\left[\frac{\ln(a/a_0)}{\sigma}\right]^2\right\}, \quad \text{for } a > a_{\text{min}}^{\text{PAH}}, \quad (3)$$

where  $\text{erf}(y) \equiv \int_0^y \exp(-x^2) dx$  is the error function. The lognormal functional form for the PAH size distribution was shown to be successful in modeling the PAH mid-IR emission spectra observed for the Milky Way diffuse interstellar medium (Li & Draine 2001b), reflection nebulae (Li & Draine 2002a), and the Small Magellanic Cloud (Li & Draine 2002b).

Lacking a priori knowledge of the balance between the photodestruction and collisional production of PAHs as a function of PAH size in the HD 141569A disk, we adopt a lower cutoff of  $a_{\text{min}}^{\text{PAH}} \equiv 3.5 \text{ \AA}$  (corresponding to  $N_C \approx 20$  for PAHs), which is the minimum survival size for PAHs in the diffuse interstellar medium (see Li & Draine 2001b). It is seen in § 4.2 that PAHs smaller than  $\sim 4.6 \text{ \AA}$  will be photochemically unstable in the inner  $r < 100 \text{ AU}$  region around the star during the lifetime of the disk. PAHs are also subject to radiative expulsion. Continuous replenishment of this material, presumably by sublimation of the icy mantles (in which interstellar PAHs have condensed during the dense molecular cloud phase) coated on the individual subgrains of large porous dust produced by collisions of large parent bodies is required to maintain the PAH disk. Therefore, it is reasonable to assume that small PAH molecules with  $a < 4.6 \text{ \AA}$  are also continuously replenished so that there exists a stable distribution of small PAHs in the disk. Since the dust (including PAHs) in the disk originates from the interstellar medium, it is thus reasonable to adopt the interstellar lower cutoff  $a_{\text{min}}^{\text{PAH}} = 3.5 \text{ \AA}$  for the PAHs in the disk. But we will also see in § 4.2 that models with  $a_{\text{min}}^{\text{PAH}} = 4.6 \text{ \AA}$  are also capable of closely reproducing the observed SED, including the PAH emission features.

### 3.1.2. Porous Dust

Large porous dust in the HD 141569A disk will attain a steady state temperature determined by balancing absorption and emission:

$$\left(\frac{R_*}{2r}\right)^2 \int_0^\infty C_{\text{abs}}^{\text{PD}}(a, \lambda) F_\lambda^* d\lambda = \int_0^\infty C_{\text{abs}}^{\text{PD}}(a, \lambda) 4\pi B_\lambda \{T[a, r]\} d\lambda, \quad (4)$$

where  $C_{\text{abs}}^{\text{PD}}(a, \lambda)$  is the absorption cross section of porous dust of spherical radius  $a$  at wavelength  $\lambda$  and  $T(a, r)$  is the equilibrium temperature of dust of size  $a$  at a radial distance  $r$  from the star.

The IR emissivity (in units of  $\text{ergs s}^{-1} \mu\text{m}^{-1}$ ) for porous dust with a size distribution of  $dn_{\text{PD}}/da$  located at a distance of  $r$  from the central star is

$$j_{\lambda}^{\text{PD}}(r) = \int_{a_{\text{min}}}^{a_{\text{max}}} da \frac{dn_{\text{PD}}}{da} 4\pi B_\lambda \{T[a, r]\} C_{\text{abs}}^{\text{PD}}(a, \lambda). \quad (5)$$

We assume a power-law dust size distribution for the porous dust:

$$\frac{dn_{\text{PD}}}{da} = \begin{cases} \frac{1}{\ln[a_{\text{max}}/a_{\text{min}}]} a^{-1}, & \alpha = 1, \\ \frac{(1-\alpha)}{a_{\text{max}}^{1-\alpha} - a_{\text{min}}^{1-\alpha}} a^{-\alpha}, & \alpha \neq 1, \end{cases} \quad (6)$$

where  $a$  is the spherical radius,  $a_{\text{min}}$  is the lower cutoff,  $a_{\text{max}}$  is the upper cutoff, and  $\alpha$  is the power-law index. We take  $a_{\text{min}} = 1 \mu\text{m}$  and  $a_{\text{max}} = 1 \text{ cm}$  (this is not a critical parameter since grains larger than  $\sim 100 \mu\text{m}$  emit like blackbodies and their IR emission spectra are size-insensitive; see Fig. 6).

We use Mie theory to calculate the absorption cross sections for porous dust. The fluffy, heterogeneous dust aggregate is represented by an equivalent homogeneous sphere with an effective dielectric function  $\epsilon_{\text{eff}}$ . Dielectric functions for the constituent dust materials are taken from (1) Draine & Lee (1984) for amorphous silicate dust; (2) Li & Draine (2001a) for crystalline silicate dust; (3) Li & Greenberg (1997) for carbonaceous dust; and (4) Li & Greenberg (1998) for H<sub>2</sub>O-dominated ice. Let  $\epsilon_{\text{sil}}$ ,  $\epsilon_{\text{carb}}$ , and  $\epsilon_{\text{ice}}$  be the complex dielectric functions of silicate (either amorphous or crystalline), carbonaceous, and ice dust, respectively. Let  $f_{\text{sil}}$ ,  $f_{\text{carb}}$ , and  $f_{\text{ice}}$  be, respectively, the volume fraction of silicate, carbonaceous, and ice dust in an aggregate, which can be obtained from the mass mixing ratio  $m_{\text{carb}}/m_{\text{sil}}$  and  $m_{\text{ice}}/(m_{\text{sil}} + m_{\text{carb}})$  and the fluffiness  $P$  ( $\equiv 1 - f_{\text{sil}} - f_{\text{carb}} - f_{\text{ice}}$ ) of the aggregate (see § 3.1). We first employ the Maxwell-Garnett effective medium theory (Bohren & Huffman 1983) to calculate the average dielectric functions for the ice-coated silicate subgrains  $\epsilon'_{\text{sil}}$  and the ice-coated carbonaceous subgrains  $\epsilon'_{\text{carb}}$ :

$$\epsilon'_{\text{sil}} = \epsilon_{\text{ice}} \frac{(1 + 2f'_{\text{sil}})\epsilon_{\text{sil}} + 2(1 - f'_{\text{sil}})\epsilon_{\text{ice}}}{(1 - f'_{\text{sil}})\epsilon_{\text{sil}} + (2 + f'_{\text{sil}})\epsilon_{\text{ice}}}, \quad f'_{\text{sil}} = \frac{f_{\text{sil}}}{f_{\text{sil}} + \xi f_{\text{ice}}}, \quad (7)$$

$$\epsilon'_{\text{carb}} = \epsilon_{\text{ice}} \frac{(1 + 2f'_{\text{carb}}P)\epsilon_{\text{carb}} + 2(1 - f'_{\text{carb}}P)\epsilon_{\text{ice}}}{(1 - f'_{\text{carb}}P)\epsilon_{\text{carb}} + (2 + f'_{\text{carb}}P)\epsilon_{\text{ice}}}, \quad f'_{\text{carb}} = \frac{f_{\text{carb}}}{f_{\text{carb}} + (1 - \xi)f_{\text{ice}}}, \quad (8)$$

where  $\xi$  is the fraction of ice condensed on the silicate cores. For the cold-coagulation dust model, we assume  $\xi = 0.5$  (i.e., in an dust aggregate, the available ice equally condenses on the silicate subgrains and on the carbonaceous subgrains); for the hot-nebula dust model, we assume  $\xi = 1$  since we assume that all carbon dust has been destroyed by oxidation (see Li & Lunine 2003). We then use the Bruggman effective medium theory (Bohren & Huffman 1983) to calculate the mean dielectric functions  $\epsilon_{\text{eff}}$  for the porous heterogeneous dust

<sup>5</sup> A fluffy grain of  $a = 1 \mu\text{m}$  with a porosity of  $P = 0.90$  consists of  $\sim 100$  constituent individual (interstellar) particles that have a typical size of  $a \sim 0.1 \mu\text{m}$  (see Li & Greenberg 1997). Models with a smaller  $a_{\text{min}} (= 0.1 \mu\text{m})$  and a larger  $a_{\text{min}} (= 10 \mu\text{m})$  are discussed in § 4.1.

aggregate:

$$(f_{\text{sil}} + \xi f_{\text{ice}}) \frac{\epsilon'_{\text{sil}} - \epsilon_{\text{eff}}}{\epsilon'_{\text{sil}} + 2\epsilon_{\text{eff}}} + [f_{\text{carb}} + (1 - \xi)f_{\text{ice}}] \frac{\epsilon'_{\text{carb}} - \epsilon_{\text{eff}}}{\epsilon'_{\text{carb}} + 2\epsilon_{\text{eff}}} + (1 - f_{\text{sil}} - f_{\text{carb}} - f_{\text{ice}}) \frac{1 - \epsilon_{\text{eff}}}{1 + 2\epsilon_{\text{eff}}} = 0, \quad (9)$$

where the third term accounts for the contribution from the vacuum ( $\epsilon = 1$ ). By definition, equations (7)–(9) are valid for both the cold-coagulation dust model ( $\xi = 0.5$ ) and the hot-nebula dust model ( $\xi = 1$ ), either with ( $f_{\text{ice}} > 0$ ) or without ( $f_{\text{ice}} = 0$ ) ice mantles.

### 3.1.3. IR Emission Spectrum

For a given dust size distribution and a given disk structure (i.e., the dust spatial density distribution), the emergent IR emission spectrum can be obtained by integrating over the dust size range and over the entire disk. Assuming an optically thin (see § 3.2) and radially symmetric disk, the flux density (in units of  $\text{ergs s}^{-1} \text{cm}^{-2} \mu\text{m}^{-1}$ ) received at the Earth is

$$F_{\lambda} = \frac{1}{4\pi d^2} \left[ \int_{r_{\text{in}}}^{r_{\text{out}}} j_{\lambda}^{\text{PD}}(r) \sigma(r) 2\pi r dr + j_{\lambda}^{\text{PAH}}(U) m_{\text{PAH}}(U) \right], \quad (10)$$

where  $d \approx 99$  pc is the distance from the star to the Earth,  $\sigma(r)$  is the surface density for the porous dust component,  $r_{\text{in}}$  and  $r_{\text{out}}$  are, respectively, the inner and outer boundaries of the disk, and  $m_{\text{PAH}}(U)$  is the total mass of the PAH dust required to account for the observed PAH IR emission bands if the PAH molecules in the HD 141569A disk are illuminated by starlight of an intensity  $U$  times that of the 912 Å–1  $\mu\text{m}$  MMP interstellar radiation field. We justify the optically thin treatment in § 3.2 (also see Table 2). The HD 141569A disk is actually asymmetric (Mouillet et al. 2001; Boccaletti et al. 2003; Clampin et al. 2003); therefore, our model, based on an assumption of a radially symmetric disk, is somewhat simplified. But this is not expected to affect the conclusion of this paper since the asymmetric dust spatial distribution, which would account for the observed brightness asymmetry, with some fine-tuning, would also be able to reproduce the observed SED, as can be seen from equation (10).

Because of their single-photon heating nature, the IR emission spectral shape of PAHs is independent of the starlight intensity  $U$ ; the absolute emissivity level simply scales with  $U$  (Draine & Li 2001; see Fig. 13 in Li & Draine 2001b). Namely,  $j_{\lambda}^{\text{PAH}}(U)/U$  remains identical over the entire dust disk, provided that the charging condition  $UT_{\text{gas}}^{1/2}/n_e$  for PAHs does not vary in the disk.<sup>6</sup> For computing the PAH component, it is therefore not necessary to integrate over the disk; instead, it is sufficient just to calculate the PAH IR emission spectrum for a single radiation intensity  $U$  (i.e., a single region  $r$  in the disk). The required PAH mass is inversely proportional to  $U$ .

<sup>6</sup> The PAH ionization fraction  $\phi_{\text{ion}}$  depends on  $U/n_e$  and  $T_{\text{gas}}$ , where  $n_e$  is the electron density in the disk and  $T_{\text{gas}}$  is the gas temperature (Weingartner & Draine 2001).

The total mass for the porous dust component is

$$m_{\text{PD}} = \int_{r_{\text{in}}}^{r_{\text{out}}} \sigma(r) 2\pi r dr \int_{a_{\text{min}}}^{a_{\text{max}}} da \frac{dn_{\text{PD}}}{da} \frac{4\pi}{3} a^3 \rho_{\text{PD}}, \quad (11)$$

where  $\rho_{\text{PD}}$  is the mass density of the porous dust component (see Appendix B in Li & Lunine 2003).

The vertical optical depth is

$$\tau_{\lambda}(r) = \int_{a_{\text{min}}}^{a_{\text{max}}} da \frac{dn_{\text{PD}}}{da} \sigma(r) C_{\text{ext}}^{\text{PD}}(a, \lambda), \quad (12)$$

where  $C_{\text{ext}}^{\text{PD}}(a, \lambda)$  is the extinction cross section of the porous dust of spherical radius  $a$  at wavelength  $\lambda$ . The optical depth from the PAH component is negligible (see § 3.2).

The dust spatial distribution is well constrained by the near-IR imaging of scattered starlight (Weinberger et al. 1999; Augereau et al. 1999a) and mid-IR imaging of dust thermal emission (Marsh et al. 2002). We adopt the following analytical formula to approximate the dust distribution that was derived from the scattered light (see Fig. 3 of Weinberger et al. 1999) and dust thermal emission (see Fig. 4 of Marsh et al. 2002)<sup>7</sup>:

$$\frac{\sigma(r)}{\sigma_p} = \begin{cases} 0.223 \exp \left[ -4 \ln 2 \left( \frac{r/\text{AU} - 55}{70} \right)^2 \right], & r_{\text{in}} < r < 105 \text{ AU}, \\ \exp \left[ -4 \ln 2 \left( \frac{r/\text{AU} - 203}{90} \right)^2 \right], & 105 \text{ AU} < r < 235 \text{ AU}, \\ \frac{0.914 \times 140^2}{(r/\text{AU} - 310)^2 + 140^2}, & 235 \text{ AU} < r < r_{\text{out}}, \end{cases} \quad (13)$$

where  $\sigma_p$  is the midplane surface density at  $r = r_p \equiv 203$  AU. We note that since we use this dust spatial distribution, it is expected that our models are also able to reproduce the imaging observations. The first line of equation (13) represents the 12.5, 17.9, and 20.8  $\mu\text{m}$  mid-IR-emitting dust component (Marsh et al. 2002). The second and third lines of equation (13) describe the two annular structures peaking at  $r \approx 200$  and 325 AU, respectively (Augereau et al. 1999a; Weinberger et al. 1999; Mouillet et al. 2001). The inner boundary  $r_{\text{in}}$  is set at where grains are heated to  $\geq 1500$  K. Therefore,  $r_{\text{in}}$  is a function of dust size. For micron-sized grains, the inner boundary is roughly at  $r_{\text{in}} = 0.2$  AU. The outer boundary is taken to be  $r_{\text{out}} = 500$  AU, which is expected from the disk truncation caused by the tidal effects of HD 141569B, a companion star of HD 141569A (Weinberger et al. 2000).<sup>8</sup> This is also consistent with the near-IR scattered light observations reported by

<sup>7</sup> We assume that the dust vertical distribution is determined by the vertical hydrostatic equilibrium (see eqs. [B2]–[B4]).

<sup>8</sup> It was shown by Artymowicz & Lubow (1994) that circumstellar disks will be truncated by the tidal effects of a companion star in circular orbit at approximately 0.9 of the average Roche lobe radius. For the HD 141569A ( $m_* \approx 2.3 m_{\odot}$ ; van den Ancker et al. 1998) and HD 141569B ( $m_* \approx 0.5 m_{\odot}$ ; Weinberger et al. 2000) system with a mass ratio of  $q \approx 4.6$ , the Roche lobe radius is  $R_{\text{cr}} \approx 0.49 A q^{2/3} / [0.6 q^{2/3} + \ln(1 + q^{1/3})] \approx 0.51 A$ , where  $A$  ( $\approx 990$  AU; Weinberger et al. 2000;  $\approx 1065$  AU; Boccaletti et al. 2003) is the physical separation between HD 141569A and HD 141569B. However, if HD 141569B is out of the HD 141569A disk plane, the physical separation  $A$  must be much larger than 990 AU. As discussed in § 4.1, models with a larger  $r_{\text{out}}$  value also provide good fits to the observed SED (see Fig. 7).

TABLE 2  
MODELS FOR THE HD 14156 9A DUST DISK IR EMISSION

Model Number	Dust Type	$P$	$P^a$	$\alpha^b$	$\langle a \rangle^c$ ( $\mu\text{m}$ )	$\langle a^2 \rangle^c$ ( $\mu\text{m}^2$ )	$\langle a^3 \rangle^c$ ( $\times 10^{-3} \text{ cm}^3$ )	$m_d$ ( $\times 10^{28} \text{ g}$ )	$\sigma_p^d$ ( $\times 10^4 \text{ cm}^{-2}$ )	$m_{\text{PAH}}^e$ ( $\times 10^{22} \text{ g}$ )	$\tau_p(V)^f$ ( $\times 10^{-2}$ )	$\chi^2/N$	Note
1.....	Cold-coagulation	0.90	0.73	3.3	1.77	7.18	0.21	2.13	4.84	4.24	2.41	1.89	Preferred
2.....	Hot-nebula	0.90	0.80	3.0	2.00	18.4	2.00	6.63	1.52	5.07	1.85	3.67	
3.....	Cold-coagulation	0.90	0.73	3.2	0.18	0.099	0.0027	2.52	430.5	4.29	2.18	2.27	$a_{\text{max}} = 0.1 \mu\text{m}$
4.....	Cold-coagulation	0.90	0.73	3.6	16.2	426.5	9.65	1.66	0.081	5.51	2.21	1.72	$a_{\text{max}} = 10 \mu\text{m}$
5.....	Cold-coagulation	0.90	0.73	3.3	1.77	7.18	0.21	3.01	4.66	4.32	2.32	1.70	$r_{\text{out}} = 1000 \text{ AU}$
6.....	Cold-coagulation	0.95	0.87	3.2	1.83	9.26	0.44	1.73	3.89	4.28	2.38	2.00	
7.....	Cold-coagulation	0.80	0.46	3.5	1.67	4.95	0.049	1.38	6.58	4.22	2.21	2.13	
8.....	Cold-coagulation	0.90	0.73	3.3	1.77	7.18	0.21	2.13	4.84	4.45	2.41	2.34	$a_0 = 3.5 \text{ \AA}, \sigma = 0.4$
9.....	Cold-coagulation	0.90	0.73	3.3	1.77	7.18	0.21	2.13	4.84	6.19	2.41	4.97	$a_0 = 3 \text{ \AA}, \sigma = 0.2, \phi_{\text{ion}} = 0.5$
10.....	Cold-coagulation	0.90	0.73	3.3	1.77	7.18	0.21	2.13	4.84	9.95	2.41	24.4	$a_0 = 3 \text{ \AA}, \sigma = 0.2, \phi_{\text{ion}} = 0$
11.....	Cold-coagulation	0.90	0.73	3.3	1.77	7.18	0.21	2.13	4.84	4.47	2.41	2.02	$a_{\text{min}}^{\text{PAH}} = 4.6 \text{ \AA}$

NOTE.—Unless otherwise stated, all models assume (1)  $a_{\text{min}} = 1 \mu\text{m}$  and  $a_{\text{max}} = 1 \text{ cm}$  for the porous dust component; (2)  $a_0 = 2.5 \text{ \AA}$ ,  $\sigma = 0.3$ ,  $a_{\text{min}}^{\text{PAH}} = 3.5 \text{ \AA}$ , and  $\phi_{\text{ion}} = 1$  for the PAH component; (3)  $r \in [0.2, 500 \text{ AU}]$  for the dust spatial distribution given in eq. (13).

<sup>a</sup> The porosity of the ice-coated porous aggregate (see Appendix B in Li & Lunine 2003).

<sup>b</sup> The index of the power-law size distribution for the porous dust component:  $dn(a)/da \sim a^{-\alpha}$  for  $a \in [a_{\text{min}}, a_{\text{max}}]$  (see eq. [6]).

<sup>c</sup>  $\langle a^i \rangle = \int_{a_{\text{min}}}^{a_{\text{max}}} da a^i dn(a)/da / \int_{a_{\text{min}}}^{a_{\text{max}}} da dn(a)/da$ . The dust surface mass density can be written as  $\sigma(r; m) = \langle m \rangle \sigma(r)$ , with the mean dust mass  $\langle m \rangle = (4\pi/3) \langle a^3 \rangle \langle \rho \rangle$ , where  $\langle \rho \rangle \approx 2.5(1 - P) \text{ g cm}^{-3}$ ,  $\langle \rho \rangle \approx 1.7(1 - P) \text{ g cm}^{-3}$  for the cold-coagulation model and  $\langle \rho \rangle \approx 3.5(1 - P) \text{ g cm}^{-3}$ ,  $\langle \rho \rangle \approx 2.4(1 - P) \text{ g cm}^{-3}$  for the hot-nebula model (see Appendix B in Li & Lunine 2003).

<sup>d</sup> The midplane surface density ( $z = 0$ ) at  $r_p = 203 \text{ AU}$  for the porous dust component (see second line of eq. [13]).

<sup>e</sup> We assume that the spatial distribution of the PAH component follows that of the inner warm porous dust (which is responsible for the 10.8 and 18.2  $\mu\text{m}$  mid-IR emission observed by Fisher et al. 2000; see Fig. 3a and eq. [13]) at  $r \lesssim 105 \text{ AU}$  (see § 3.1.3).

<sup>f</sup> The vertical optical depth at  $\lambda = 0.55 \mu\text{m}$  and  $r_p = 203 \text{ AU}$ . The contribution to  $\tau(V)$  from the PAH component is negligible (see § 3.2).

Weinberger et al. (1999) and Augereau et al. (1999a), which show that the HD 141569A disk extends to a radial distance of about 500 AU.

The mean starlight intensity  $\langle U \rangle$ , averaged over the different portions of the disk and weighted by the surface density of the porous dust population, is

$$\langle U \rangle = \frac{\int_{r_{\text{in}}}^{r_{\text{out}}} U(r) \sigma(r) 2\pi r dr}{\int_{r_{\text{in}}}^{r_{\text{out}}} \sigma(r) 2\pi r dr} \approx \begin{cases} 1.24 \times 10^6, & r_{\text{in}} = 1 \text{ AU} < r < 105 \text{ AU}, \\ 2.76 \times 10^4, & 105 \text{ AU} < r < r_{\text{out}} = 500 \text{ AU}, \\ 4.03 \times 10^4, & r_{\text{in}} = 1 \text{ AU} < r < r_{\text{out}} = 500 \text{ AU}. \end{cases} \quad (14)$$

PAHs smaller than  $\sim 4.6 \text{ \AA}$  will be photodestroyed in a timescale shorter than the age of the HD 141569A system (see § 4.2). PAHs will also be efficiently removed from the disk by radiation pressure (see § 4.3). Therefore, the PAH component in the HD 141569A disk must be continuously replenished, most likely through the evaporation of the icy mantles<sup>9</sup> of grains produced by the breakup of larger bodies. The evaporation of icy mantles takes place at  $r < 100 \text{ AU}$  for micron-sized dust and at  $r < 30 \text{ AU}$  for millimeter-sized dust (see Fig. 6). Therefore, it is reasonable to assume that the free-flying PAH molecules, responsible for the observed PAH IR emission bands, are mainly distributed in the inner  $r < 100 \text{ AU}$  region. If we assume that the spatial distribution of PAHs follows that of the porous dust at  $r < 100 \text{ AU}$ , the mean starlight intensity to which the PAHs in the HD 141569A disk are exposed is  $\langle U \rangle \approx 1.24 \times 10^6$  (see eq. [14]).

### 3.1.4. PAH Ionization

PAHs acquire charge through photoelectric emission and collisions with electrons and ions. Ideally, one can calculate the steady state charge distribution for a PAH molecule of radius  $a$  from the balance between the electron capture rates and the photoelectron emission rates plus the ion capture rates (see, e.g., Weingartner & Draine 2001). Since little is known regarding the electron density  $n_e$  and its distribution in the HD 141569A disk, we do not carry out detailed calculations of the PAH charge distribution; instead, we just calculate and compare the photoionization rates ( $k_{\text{ion}}$ ; see Appendix A) and the electron recombination rates ( $k_{\text{rec}}$ ; see Appendices A and B) for PAHs as a function of size and distance from the central star.

In Figure 2 we present the photoionization timescales  $\tau_{\text{ion}}$  ( $\equiv 1/k_{\text{ion}}$ ) for PAHs of various sizes at three characteristic distances  $r = 20, 55,$  and  $90 \text{ AU}$  (corresponding to the maximum and half-maximums of the PAH distribution; see eq. [13]), calculated from the method described in Appendix A. It is seen in Figure 2 that  $\tau_{\text{ion}}$  decreases as PAHs become larger and as PAHs are closer to the central star. The former is because when PAHs become larger, their ionization

<sup>9</sup> PAHs are abundant and widespread in the interstellar medium (see Léger & Puget 1984; Allamandola, Tielens, & Barker 1985; Li & Draine 2001b). It is expected that the icy mantles of the grains in dust disks, formed from condensation of volatile molecular species in the dense cloud phase, contain a substantial amount of PAHs since the freeze-out of PAHs onto the icy mantles is also expected to occur in the dense cloud phase and during the aggregation process.

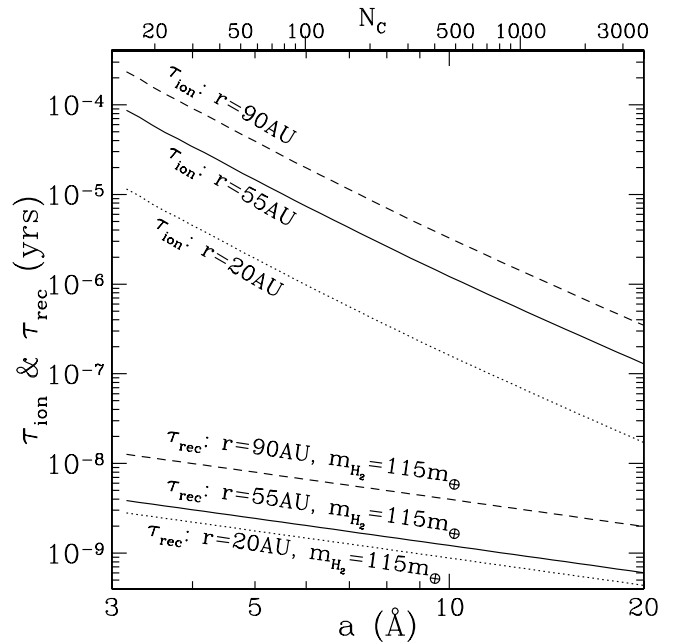


FIG. 2.—Photoionization ( $\tau_{\text{ion}}$ ; upper part of this figure; see Appendix A) and electron recombination ( $\tau_{\text{rec}}$ ; lower part; see Appendices A and B) timescales for PAHs in the size range of  $3 \text{ \AA} < a < 20 \text{ \AA}$  at  $r = 20 \text{ AU}$  (dotted lines),  $55 \text{ AU}$  (solid lines), and  $90 \text{ AU}$  (dashed lines). In calculating the electron recombination timescales, the electron density  $n_e$  is estimated from the molecular hydrogen mass determined by Zuckerman et al. (1995), assuming that the cosmic-ray ionization of  $\text{H}_2$  is the dominant contributor to the electrons in the HD 141569A disk. The upper axis indicates the number of C atoms  $N_C$  in a PAH molecule.

thresholds  $E_{\text{IP}}$  decrease (see eq. [A6]) and their UV/visible absorption cross sections increase so that their photoionization rates increase (see eq. [A7]). The latter is because, closer to the illuminating star, the UV radiation field is more intense ( $\tau_{\text{ion}} \propto r^2$ ; see eq. [A7]).

Assuming that the source of the electrons in the HD 141569A disk is dominated by the cosmic-ray ionization of  $\text{H}_2$  and adopting a total  $\text{H}_2$  mass of  $m_{\text{H}_2} \approx 115 m_{\oplus}$  inferred from submillimeter measurements of CO (Zuckerman, Forveille, & Kastner 1995), we calculate the electron recombination timescales  $\tau_{\text{rec}}$  ( $\equiv 1/k_{\text{rec}}$ ; see Appendix B for details). As shown in Figure 2, the electron recombination timescales are  $\sim 3$  orders of magnitude smaller than  $\tau_{\text{ion}}$ . Therefore, PAHs in the HD 141569A disk will be negatively charged.

### 3.1.5. Model Parameters

We have two sets of parameters to be specified or constrained:

1. The parameters  $m_{\text{PAH}}$ ,  $\phi_{\text{ion}}$ ,  $a_0$ , and  $\sigma$  determining the abundance, ionization fraction, and size distribution, respectively, of the PAH “lognormal” population (see eqs. [2], [3], and [10]).

2. The parameters  $\sigma_p$ ,  $P$ , and  $\alpha$  determining the abundance, fluffiness, and size distribution, respectively, of the porous dust population (see eqs. [6], [9], [10], and [13]).

For a given set of  $a_0$  and  $\sigma$ , the total amount of PAH dust  $m_{\text{PAH}}$  is determined by the absolute level of the observed PAH flux density (see eqs. [2], [3], and [10]). Since little is known regarding the electron density  $n_e$  and its distribution

in the disk, it is impossible to perform accurate calculations on  $\phi_{\text{ion}}$ . But we have seen in § 3.1.4 that PAHs in the HD 141569A disk will be negatively charged by capturing electrons from the cosmic-ray ionization of  $\text{H}_2$ . Since we do not distinguish the IR properties of  $\text{PAH}^-$  anions from  $\text{PAH}^+$  cations (Li & Draine 2001b),<sup>10</sup> it is appropriate to take  $\phi_{\text{ion}} = 1$ . But we will also consider models with  $\phi_{\text{ion}} = 0.5$  and 0 (see § 4.1 and Figs. 8*b* and 8*c*).

As shown in Li & Greenberg (1998) and Li & Lunine (2003), cometary-type porous dust with  $P \simeq 0.90$  is able to reproduce the observed SEDs from the IR to millimeter for the disks around the MS star  $\beta$  Pic and the pre-MS star HR 4796A; therefore, we start with  $P = 0.90$  in modeling the HD 141569A SED, but models with larger  $P$  or smaller  $P$  will also be discussed (see § 4.1 and Fig. 7).

It is interesting to note that, as early as 1965, based on a Monte Carlo simulation, Cameron & Schneck (1965) showed that a very open structure (“fairy castle”) with a porosity in the range of  $0.83 \lesssim P \lesssim 0.89$  (Cameron & Schneck 1965 used the term “*underdense*”) is expected for dust aggregates assembled from randomly incident particles, depending on their shapes, sizes, and incidence angles (also see Cameron 1995). A porosity of  $P \approx 0.90$  for the cold-coagulation dust [which implies a mass density of  $\approx 1.7 \times (1 - P') \text{ g cm}^{-3} \approx 0.46 \text{ g cm}^{-3}$  for this dust assuming ice mantles coated on the individual subgrains ( $P' \approx 0.73$ ); see Appendix B in Li & Lunine 2003] is consistent with the mean mass density  $\approx 0.5 \text{ g cm}^{-3}$  of cometary nuclei determined from studies of comet splitting and of nongravitational forces (Rickman 2003; Whipple 1999). Comets are likely to have been formed initially through the cold accumulation of interstellar dust (see, e.g., Greenberg & Li 1999). Hence, the ice-coated cold-coagulation dust aggregates we consider here are plausible building blocks of cometesimals and, hierarchically, comets.

Similar to the PAH mass parameter  $m_{\text{PAH}}$ , for a given set of  $P$  and  $\alpha$ , the total amount of porous dust (characterized by  $\sigma_p$ ; see eqs. [11] and [13]) is determined by the absolute level of the observed flux density at wavelengths  $\lambda \gtrsim 10 \mu\text{m}$ .

Therefore, we are left with  $N_{\text{par}} = 3$  adjustable parameters:  $a_0$ ,  $\sigma$ , and  $\alpha$ .

For a model with  $N_{\text{par}}$  adjustable parameters, the goodness of fit is measured by

$$\frac{\chi^2}{\text{dof}} = \frac{\sum_{i=1}^{105} [(\lambda F_\lambda)_{\text{mod}} - (\lambda F_\lambda)_{\text{obs}}]^2 / (\lambda \Delta F_\lambda)_{\text{obs}}^2}{N_{\text{par}} + 105}, \quad (15)$$

where  $(\lambda F_\lambda)_{\text{mod}}$  is the model spectrum (see eq. [10]) and  $(\lambda F_\lambda)_{\text{obs}}$  is the (dereddened, stellar photospheric contributions subtracted) observational spectrum, which includes the 10 *IRAS*, *OSCIR*, *MIRLIN*, and *SCUBA* photometric

<sup>10</sup> It has been shown that the IR properties of PAH anions closely resemble those of PAH cations (see, e.g., Szczepanski, Wehlburg, & Vala 1995; Langhoff 1996; Hudgins et al. 2000) except for the very strong  $3.3 \mu\text{m}$  C-H stretch enhancement in the anion (Szczepanski et al. 1995; Hudgins et al. 2000). However, Bauschlicher & Bakes (2000) predict that  $\text{PAH}^-$  anions have band strengths intermediate between those of neutrals (strong  $3.3 \mu\text{m}$  C-H stretching and  $11.3$ ,  $11.9$ , and  $12.7 \mu\text{m}$  out-of-plane C-H bending modes) and  $\text{PAH}^+$  cations (strong  $6.2$  and  $7.7 \mu\text{m}$  C-C stretching and  $8.6 \mu\text{m}$  C-H in-plane bending mode). In any case, the detailed differences in the band strengths between  $\text{PAH}^-$  anions and  $\text{PAH}^+$  cations would not alter our conclusions since, as shown in § 4.1, models containing a fraction ( $< 50\%$ ) of neutral PAHs are also capable of fitting the observed PAH mid-IR spectrum (see Figs. 8*b* and 8*c*).

data points and the 95 CGS3 spectroscopic data points (see Table 1), where  $(\lambda F_\lambda)_{\text{obs}}$  is the observational flux uncertainty (see Table 1 and references therein).

### 3.2. Model Results

We first consider the cold-coagulation dust model. As shown in Figure 3, our best-fit model (model 1) provides an excellent fit to the entire spectrum (including both the broadband photometry and the PAH emission features) with emission from a mixture of PAH cations ( $\phi_{\text{ion}} = 1$ ) and porous dust with a porosity of  $P = 0.90$ , a power-law size distribution index of  $\alpha \approx 3.3$ , and a total dust mass of  $m_d \approx 3.56 m_\oplus$ . The PAH component is characterized by  $a_0 \approx 2.5 \text{ \AA}$ ,  $\sigma \approx 0.3$ , and  $m_{\text{PAH}} \approx 7.10 \times 10^{-6} m_\oplus$ . See Table 2 for a full set of model parameters. For the sake of convenience, hereafter we call this model the “canonical cold-coagulation model.”

To illustrate the contributions to the observed IR emission from dust in different regions, we show in Figure 3*a* the IR emission from warm dust in the inner region of  $r < 105 \text{ AU}$  and from cool dust in the inner ( $105 \text{ AU} < r < 235 \text{ AU}$ ) and outer ( $235 \text{ AU} < r < 500 \text{ AU}$ ) rings. While the cool dust in the two rings dominates the emission at  $\lambda \gtrsim 60 \mu\text{m}$  and accounts for  $\approx 80\%$  of the  $25 \mu\text{m}$  *IRAS* flux (it is the dust in the outer ring that is responsible for the  $1350 \mu\text{m}$  *SCUBA* emission), the mid-IR  $10.8$  and  $18.2 \mu\text{m}$  radiation detected by the Keck II *OSCIR* instrument (Fisher et al. 2000; filled triangles in Fig. 3) is exclusively emitted by warm dust at  $r < 105 \text{ AU}$ . This confirms the earlier work of Fisher et al. (2000) and Augereau et al. (1999a), who suggested the existence of two separate populations of dust grains in the HD 141569A disk: inner, warmer grains that emit the mid-IR ( $10$  and  $18 \mu\text{m}$ ) radiation and more distant grains that are responsible for the scattered near-IR flux seen in the *NICMOS* images and the far-IR ( $60$  and  $100 \mu\text{m}$ ) emission detected by *IRAS*. It is worth noting that in our model, the  $r < 105 \text{ AU}$  warm dust fully accounts for both the  $10.8$  and the  $18.2 \mu\text{m}$  emission, with very little contribution from the PAH component (also see Fig. 3*b*). This is consistent with the discovery of Fisher et al. (2000) that the emitting regions at both wavelengths are of comparable size, and therefore the same population of dust may emit both the  $10.8$  and  $18.2 \mu\text{m}$  radiation.

Our model yields a total dust IR flux of  $\int_{912 \text{ \AA}}^{\infty} F_\lambda d\lambda \approx 5.89 \times 10^{-10} \text{ ergs s}^{-1} \text{ cm}^{-2}$ , corresponding to an IR luminosity of  $\sim 0.18 L_\odot$ ,  $\sim 8.1 \times 10^{-3}$  of the total stellar luminosity ( $L_* \approx 22.4 L_\odot$ ). The fractional contributions of the PAH component, the inner warm dust component, the inner ring, and the outer ring (see Fig. 3*a*) are approximately 12%, 26%, 25%, and 37%, respectively.

Our model predicts a vertical optical depth at visible wavelengths of  $\tau(V) \approx 0.024$  at  $r_p = 203 \text{ AU}$  (see Table 2). The vertical optical depths at other radial distances are smaller than this, as can be seen from equations (12) and (13). The in-plane optical depth is also much smaller than 1.<sup>11</sup> This justifies the optically thin treatment employed in the entire paper. The PAH component causes little extinction: its contribution to the visual vertical optical depth

<sup>11</sup> The in-plane optical depth can be calculated from  $\tau_\lambda \equiv \int_{r_{\text{in}}}^{r_{\text{out}}} \sigma(r) / [(2\pi)^{1/2} H(r)] dr \int_{a_{\text{min}}}^{a_{\text{max}}} C_{\text{ext}}^{\text{PD}}(a, \lambda) (dn_{\text{PD}}/da) da$ , where  $H$  is the vertical scale height (see eq. [B4]). Our best-fit model leads to  $\tau(V) \approx 0.097$ .

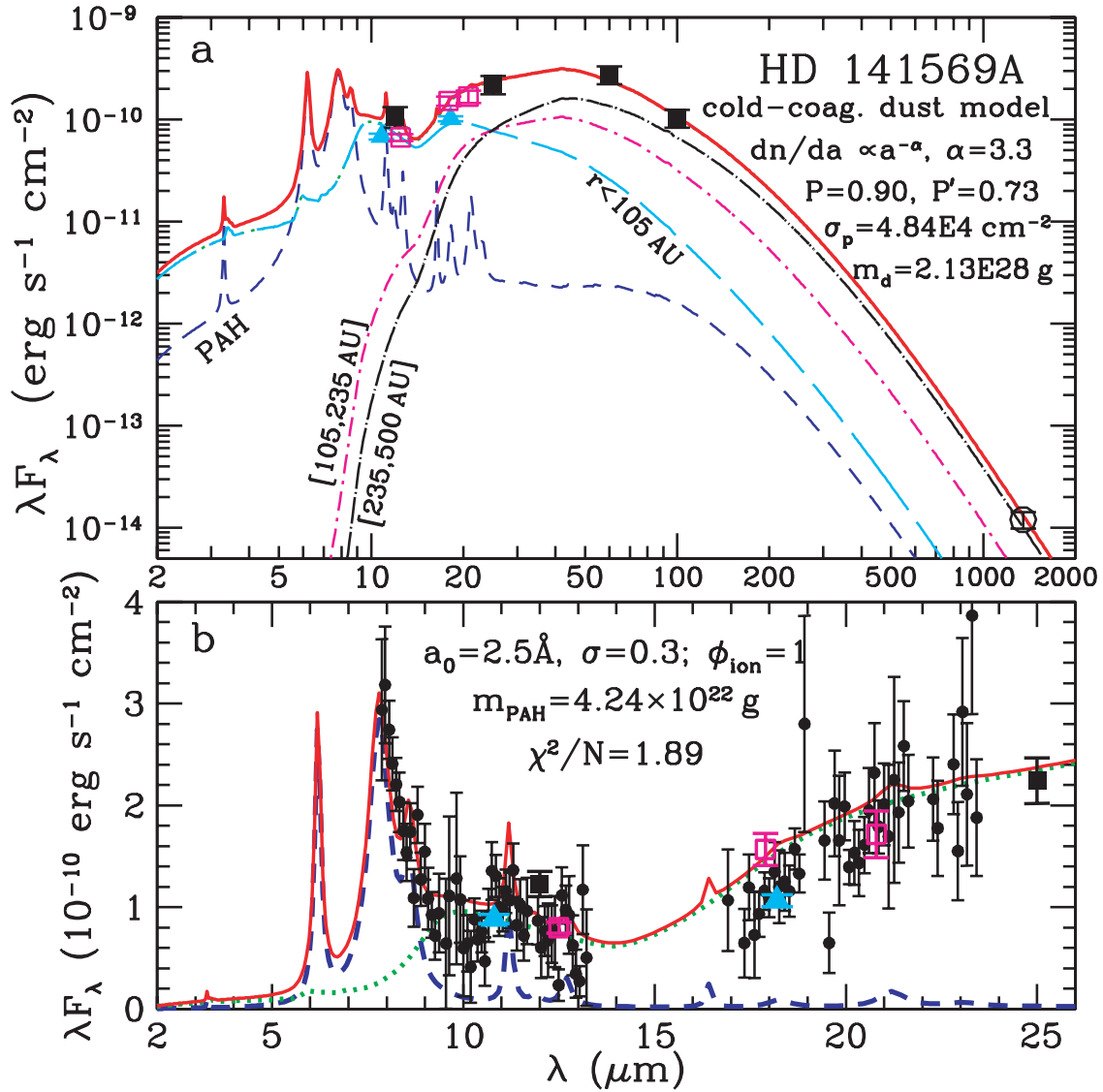


FIG. 3.—Comparison of the cold-coagulation dust model spectrum (red solid line; model 1) with the observed SED. The model consists of two dust components: (1) the PAH cation component ( $\phi_{ion} = 1$ ; blue dashed line) with a lognormal size distribution (and a lower cutoff of  $a_{min}^{PAH} = 3.5$  Å) characterized by a peak parameter of  $a_0 = 2.5$  Å, a width parameter of  $\sigma = 0.3$ , and a total mass of  $m_{PAH} \approx 7.10 \times 10^{-6} m_\oplus$ , and (2) the porous dust component (green dotted line) characterized by a porosity of  $P = 0.90$  ( $P' \approx 0.73$ ), a power-law index of  $\alpha \approx 3.3$  for the dust size distribution ( $a \in [1 \mu\text{m}, 1 \text{cm}]$ ), a dust surface density of  $\sigma_p \approx 4.84 \times 10^4 \text{cm}^{-2}$ , and a total mass of  $m_d \approx 3.56 m_\oplus$ . We adopt the dust spatial distribution ( $0.2 \text{AU} < r < 500 \text{AU}$ ) derived from imaging observations of scattered light and dust thermal emission (see eq. [13] and § 3.1.3). (a) Regional contributions of the porous dust in the inner warm region ( $r < 105 \text{AU}$ ; cyan long-dashed line), the inner ring ( $105 \text{AU} < r < 235 \text{AU}$ ; magenta dot-dashed line), and the outer ring ( $235 \text{AU} < r < 500 \text{AU}$ ; black dot-long-dashed line). The observational SED includes the 10.8 and 18.2  $\mu\text{m}$  Keck II OSCIR photometry (cyan filled triangles; Fisher et al. 2000), the 12, 25, 60, and 100  $\mu\text{m}$  IRAS photometry (black filled squares; Sylvester et al. 1996), the 12.5, 17.9, and 20.8  $\mu\text{m}$  Keck II MIRLIN photometry (magenta open squares; Marsh et al. 2002), and the CGS3 mid-IR spectrum (black filled circles in [b]), which illustrates the PAH emission bands; Sylvester et al. 1996). All observational data in (a) and (b) have been dereddened, with the stellar photospheric contribution subtracted.

at  $r = 55 \text{AU}$ , where the distribution of PAHs in the HD 141569A disk peaks (see § 3.1.3), is only  $\tau(V) \approx 1.54 \times 10^{-4}$ .<sup>12</sup>

<sup>12</sup> At first glance, one may argue that the PAH optical depth at visual wavelengths would also be about 12% of the total since the PAH component emits  $\sim 12\%$  of the total flux, so that it must have absorbed  $\sim 12\%$  of the total stellar radiation. We remind the reader that in our model the PAH dust lies closer to the star ( $r < 105 \text{AU}$ ) so that it is exposed to a radiation field  $\approx 1.24 \times 10^6 / 4.03 \times 10^4 \approx 31$  times stronger than that of the porous dust component (see eq. [14] and § 3.1.3). Another reason lies in the fact that PAHs absorb more efficiently in the UV compared to visible than do micron-sized silicate or carbon grains (see Fig. 2 in Li & Draine 2001b; Fig. 1 in Li & Draine 2002a; Figs. 4a and 5a in Draine & Lee 1984).

Similar results are obtained for the hot-nebula dust model. We show in Figure 4 the best-fit  $P = 0.90$  ( $P' \approx 0.80$ ) hot-nebula dust model spectrum (model 2; see Table 2 for model parameters). In comparison with the observed SED, the overall fit is acceptable except that the model predicts a strong crystalline silicate emission band at 21  $\mu\text{m}$ , which is not seen in the CGS3 spectrum (Sylvester et al. 1996), suggesting that only a small fraction of the hot silicate dust is in crystalline form. One should keep in mind that the cold-coagulation model and the hot-nebula model represent two extremes; the actual dust in the HD 141569A disk is likely to be somewhere intermediate between these two types. Therefore, we consider a dust model consisting of

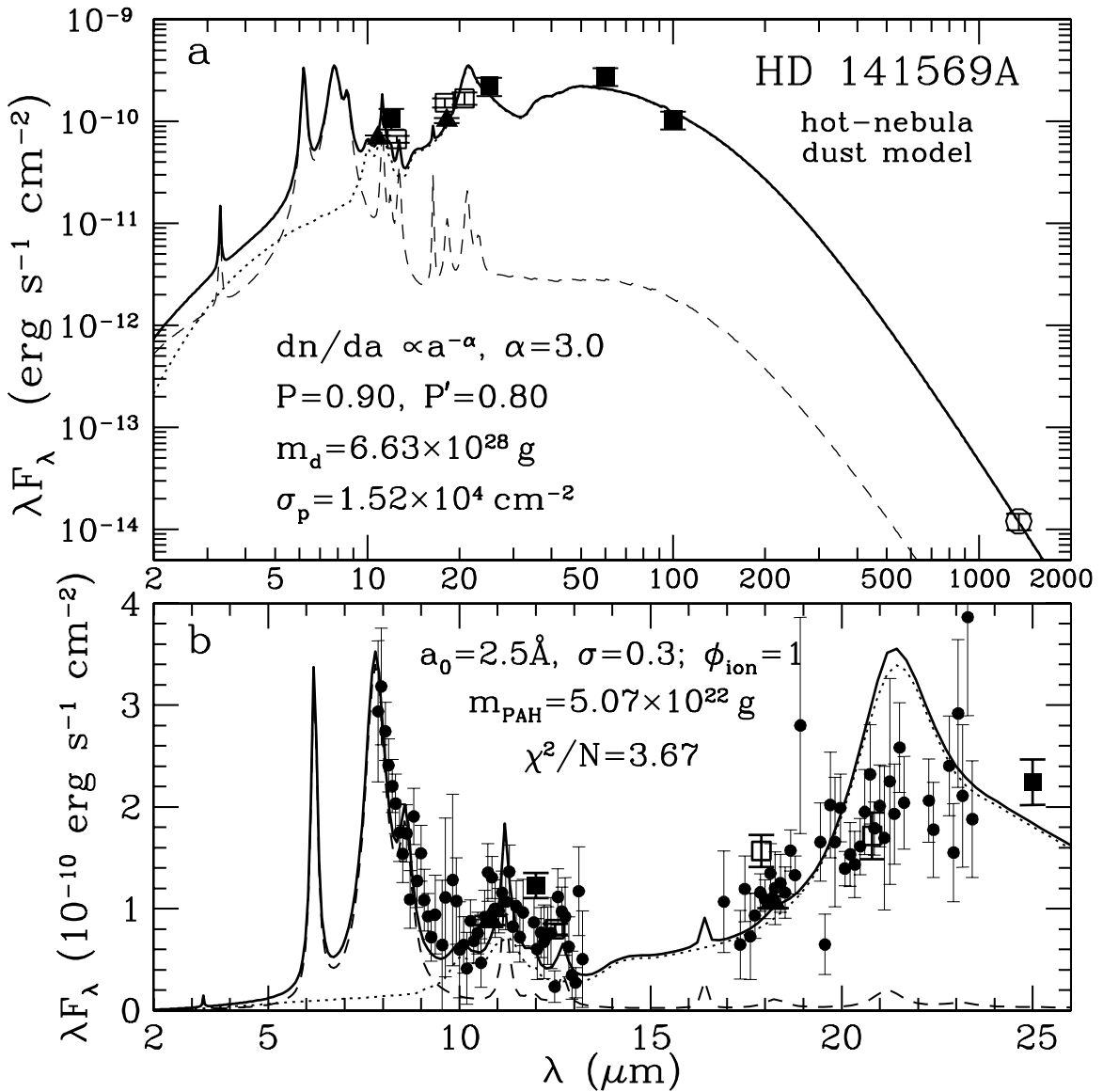


FIG. 4.—Same as Fig. 3, but for the  $P = 0.90$  ( $P' \approx 0.80$ ) hot-nebula dust model (model 2). This model predicts a broad prominent feature at  $21 \mu\text{m}$  due to crystalline silicates, which is not seen in the CGS3 spectrum (Sylvester et al. 1996).

a mixture of these two dust types with various mass mixing ratios.<sup>13</sup> Let  $f_{\text{hn}}$  be the mass fraction of the hot-nebula dust in the mixture of highly processed dust and “unaltered” dust. Let  $(\lambda F_\lambda/m_d)_{\text{cc}}$  and  $(\lambda F_\lambda/m_d)_{\text{hn}}$  be, respectively, the IR flux per gram of cold-coagulation dust (model 1) and hot-nebula dust (model 2). Let  $m_d^{\text{cc}}$  and  $m_d^{\text{hn}}$  be, respectively, the dust mass required for the cold-coagulation model (model 1) and the hot-nebula model (model 2) to reproduce the observed SED. The model spectrum expected from a mixture of these two kinds of dust with a mixing mass fraction of  $f_{\text{hn}}$  is simply

$$\lambda F_\lambda = \left[ (1 - f_{\text{hn}}) \left( \frac{\lambda F_\lambda}{m_d} \right)_{\text{cc}} + f_{\text{hn}} \left( \frac{\lambda F_\lambda}{m_d} \right)_{\text{hn}} \right] \times [(1 - f_{\text{hn}}) m_d^{\text{cc}} + f_{\text{hn}} m_d^{\text{hn}}]. \quad (16)$$

<sup>13</sup> For simplicity, we assume that they are separate populations. In reality, it is more likely that the highly processed hot-nebula dust and the “unaltered” protostellar interstellar dust are mixed to some extent and hence form porous, heterogeneous aggregates.

In Figure 5 we plot the model spectra with  $f_{\text{hn}} = 10\%$ ,  $20\%$ , and  $30\%$ . As can be seen in Figure 5b, the nondetection of the  $21 \mu\text{m}$  crystalline silicate feature places an upper limit of  $f_{\text{hn}} \approx 10\%$ .

Finally, we present in Figure 6 the equilibrium temperatures for the best-fit cold-coagulation dust ( $P = 0.90$ ,  $P' \approx 0.73$ ) and hot-nebula dust ( $P = 0.90$ ,  $P' \approx 0.80$ ) as a function of grain size at distances of  $r = 55$  and  $203$  AU from HD 141569A and  $r = 70$  AU from HR 4796A.

#### 4. DISCUSSION

The narrow, ringlike structure was originally suggested by Sylvester & Skinner (1996) for the HD 141569A disk in modeling the *IRAS* data (plus the JCMT upper limit at  $\lambda = 1.1$  mm). However, their best-fitting models required a huge inner cavity with a radius of  $\geq 670$  AU. On the other hand, it was shown by Malfait, Bogaret, & Waelkens (1998) that a flat, conventional disk extending from  $\sim 7$  to  $\sim 1400$

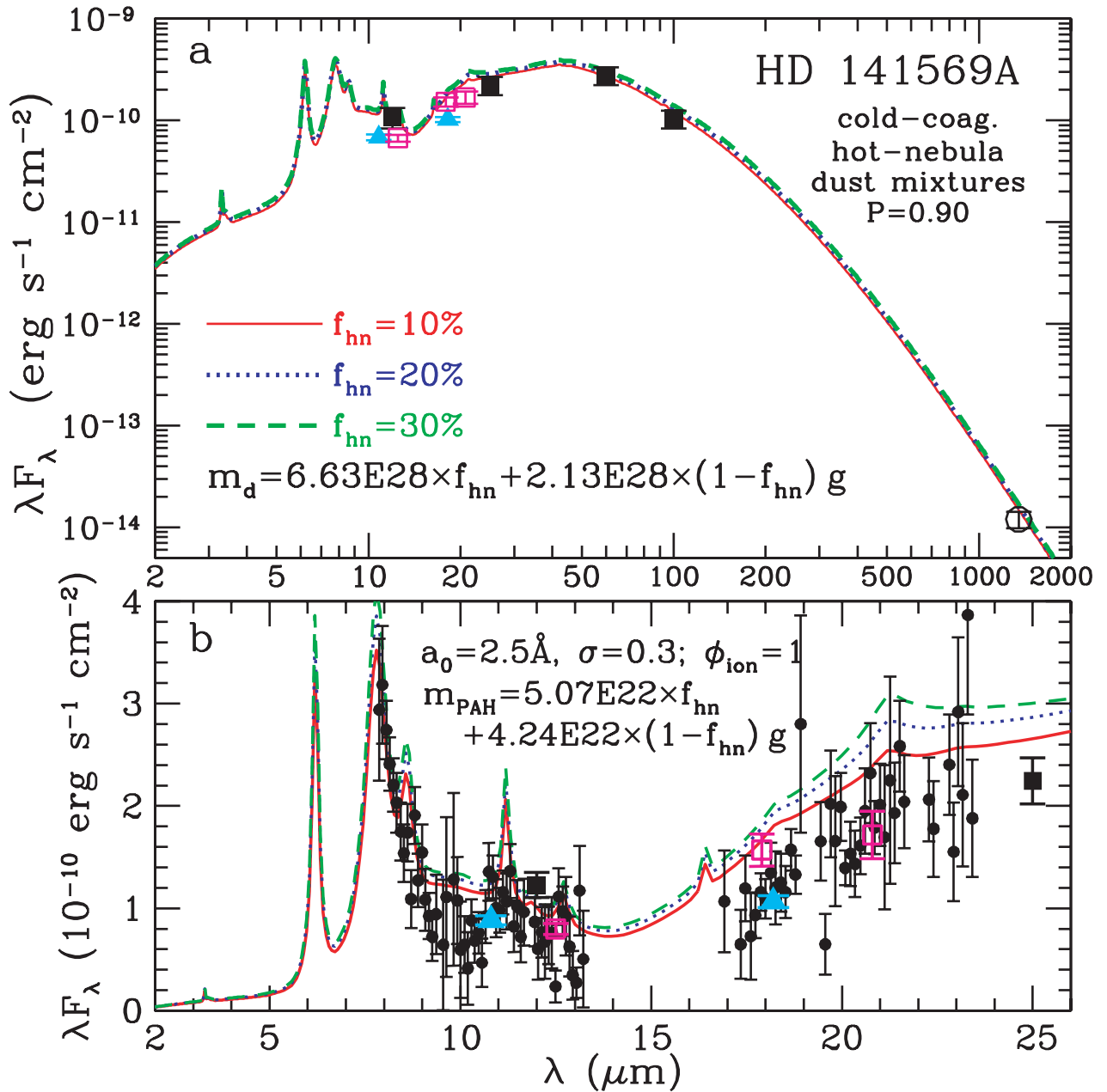


FIG. 5.—Model spectra expected from a mixture of the cold-coagulation dust (model 1; Fig. 3) with a mass fraction of  $(1 - f_{\text{hn}})$  and the hot-nebula dust (model 2; Fig. 4) with a mass fraction of  $f_{\text{hn}}$  (red solid line:  $f_{\text{hn}} = 10\%$ ; blue dotted line:  $f_{\text{hn}} = 20\%$ ; green dashed line:  $f_{\text{hn}} = 30\%$ ). The nondetection of the  $21 \mu\text{m}$  crystalline silicate feature limits the fraction of hot-nebula dust (i.e., crystalline silicates) to  $f_{\text{hn}} \approx 10\%$ .

AU with a power-law index of  $-0.6$  for the dust spatial distribution was also able to fit the *IRAS* data.

Malfait et al. (1998) modeled the HD 141569A *IRAS* data in terms of dust with a hypothetical opacity law of  $\kappa_{\text{abs}} \propto \lambda^{-1}$  and a hypothetical radial-dependent temperature of  $T_{\text{d}}(r) = 6180(r/R_{*})^{-2/5}$  K. Their inferred dust spatial distribution of  $dn(r)/dr \propto r^{-0.6}$  with  $r \in [7, 1400 \text{ AU}]$  is inconsistent with the current view of a central void at  $r \gtrsim 20$  AU (see, e.g., Marsh et al. 2002; Mouillet et al. 2001). In the work of Sylvester & Skinner (1996), the dust in the HD 141569A disk was modeled as either a mixture of two separate components (amorphous silicate and amorphous carbon) or a single pure amorphous carbon component. The

dust was taken to be compact spheres with a power-law size distribution of  $dn/da \sim a^{-3.5}$  in the size range  $50 \text{ \AA} < a < 100 \mu\text{m}$ . The variation of dust density within the disk with distance from the star (i.e.,  $dn/dr$ ) was also treated as a power law. Their model did not treat the PAH emission bands. It is therefore not surprising that their model spectrum was deficient at  $\lambda \lesssim 15 \mu\text{m}$ .

Using the Keck II OSCIR  $10.8$  and  $18.2 \mu\text{m}$  flux ratio, Fisher et al. (2000) placed an upper limit of  $a_{\text{max}} \simeq 1 \mu\text{m}$  on the radius of the dust grains responsible for the mid-IR emission at *both* wavelengths if they are made of compact silicate spheres. Since this conclusion was drawn from the assumption that the dust is located at a distance of  $20$  AU

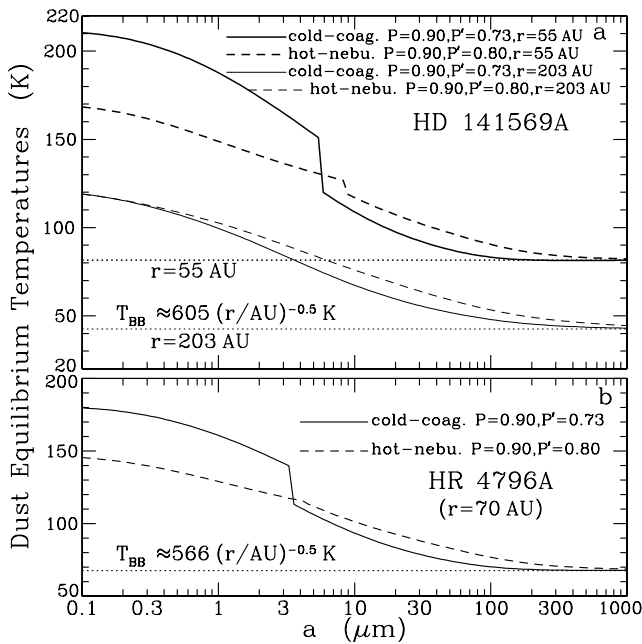


FIG. 6.—Equilibrium temperatures for cold-coagulation dust of  $P = 0.90$  ( $P' \approx 0.73$ ) from (a) HD 141569A at a distance of  $r = 55$  AU (solid line) and  $r = 203$  AU (thin solid line), from (b) HR 4796A at  $r = 70$  AU (solid line), and for hot-nebula dust of  $P = 0.90$  ( $P' \approx 0.80$ ) from (a) HD 141569A at  $r = 55$  AU (dashed line) and  $r = 203$  AU (thin dashed line), and from (b) HR 4796A at  $r = 70$  AU (dashed line). The horizontal dotted lines plot the blackbody temperatures from (a) HD 141569A of  $T_{\text{BB}} \approx 81.6$  and  $42.5$  K, respectively, at  $r = 55$  and  $203$  AU and from (b) HR 4796A of  $T_{\text{BB}} \approx 67.6$  K at  $r = 70$  AU. The discontinuity at  $T \approx 120$  K in the temperature profiles (as a function of grain size) results from ice sublimation: grains hotter than  $\sim 120$  K do not maintain icy mantles and therefore attain higher temperatures than their icy counterpart since silicate and carbon materials have a much higher UV/visual absorptivity than  $\text{H}_2\text{O}$ -dominated ice.

from the star, a wide range of grain sizes may be allowed if the mid-IR emitting dust is widespread within  $r < 105$  AU (see eq. [13]).

In contrast, a lower limit of  $a_{\text{min}} \approx 0.6 \pm 0.2 \mu\text{m}/(1 - P)$  was derived by Boccaletti et al. (2003) for grains with a porosity of  $P$ , assuming that the slight surface brightness difference between their ground-based  $2.2 \mu\text{m}$  imaging data and the *HST* NICMOS data at  $1.1 \mu\text{m}$  (Weinberger et al. 1999) and  $1.6 \mu\text{m}$  (Augereau et al. 1999a) is caused by the color effect of the grains. A grain size distribution steeper than  $dn/da \propto a^{-3}$  was also inferred from such an analysis. However, these conclusions are very sensitive to the scaling factor between the target star and the calibrator star, which is uncertain. Once the scaling factor uncertainty is included in their analysis, a much wider range of grain sizes is allowed.

In comparison with the narrow, sharply bounded HR 4796A disk (Schneider et al. 1999), the dust annulus around HD 141569A is about 9–10 times wider and displays a more complex ring-gap-ring morphology (Augereau et al. 1999a; Weinberger et al. 1999; Clampin et al. 2003). In addition, for the HD 141569A disk, there is clear evidence for the existence of a warm dust population at  $r < 105$  AU inward of the inner ring (Marsh et al. 2002). While a warm “zodiacal” dust component at a radial distance of a few AU from HR 4796A was invoked by Koerner et al. (1998) and Augereau et al. (1999b) to account for the emission at  $\lambda \lesssim 12 \mu\text{m}$ , it was shown later by Li & Lunine (2003) that the porous dust model naturally explains the entire dust emission including that at  $\lambda \lesssim 12 \mu\text{m}$ , and, therefore, there does not seem to be any strong evidence for a zodiacal dust component in the inner disk of HR 4796A. Very recently, Marsh et al. (2002) found that the radial optical depth profile of the HD 141569A disk at  $\lambda = 12.5 \mu\text{m}$  appears to increase inside of  $r = 20$  AU at a  $2\sigma$  level. Does this indicate the existence of a zodiacal dust component in the HD 141569A disk? *SIRTF* imaging at the 3.6, 4.5, and  $5.8 \mu\text{m}$  IRAC bands (see Table 3 and § 4.4) may be able to address this question since the zodiacal dust may also reveal its existence by emitting at the IRAC bands. It is interesting to note that the *M*-band ( $4.77 \mu\text{m}$ ) photometry does appear to show a small excess over the stellar photosphere (see Fig. 1a). But the uncertainties in both the photometric flux determination and the Kurucz model atmosphere representation prevent a definite conclusion.

The time for complete sublimation of the ice mantles coated on the individual tenth-micron subgrains of a porous aggregate of temperature  $T$  (see Fig. 6) is

$$\tau_{\text{subl}} \approx 1.5 \times 10^{-12} (\Delta a / \mu\text{m}) (\rho_{\text{ice}} / \text{g cm}^{-3}) \times 10^{(2480\text{K}/T)} (T/\text{K})^{-3.5} \text{ yr}$$

(Backman & Paresce 1993), where  $\Delta a \approx 0.04 \mu\text{m}$  is the ice mantle thickness. By integrating  $\tau_{\text{subl}}$  over the dust size distribution  $dn_{\text{PD}}/da$ , we estimate the mean sublimation time-scales to be  $\langle \tau_{\text{subl}} \rangle \approx 7.6 \times 10^5$ ,  $3.3 \times 10^{32}$ , and  $2.8 \times 10^{10}$  yr, respectively, for the best-fit cold-coagulation dust at distances of  $r = 55$  and  $203$  AU from HD 141569A and  $70$  AU from HR 4796A. If PAHs in dust disks indeed originate from the sublimation of icy mantles, we expect to see PAHs in the inner warm region of the HD 141569A disk ( $r < 100$  AU), where  $\tau_{\text{subl}} < \tau_{\text{age}}$ , but not in the ring regions of the HD 141569A ( $r > 100$  AU) and HR 4796A disks ( $r \gtrsim 70$  AU), where  $\tau_{\text{subl}} \gtrsim \tau_{\text{age}}$ .

The 3.3, 6.2, 7.7, 8.6, and  $11.3 \mu\text{m}$  vibrational band diagnostics of PAH molecules are not seen in the HR 4796A disk. As mentioned above, this is mainly because in the  $r = 70$  AU ring region, the sublimation of icy mantles that

TABLE 3  
DUST IR EMISSION (Jy) INTEGRATED OVER *SIRTF* BANDS PREDICTED FOR OUR PREFERRED MODELS

Model Number	IRAC 3.6 $\mu\text{m}$	IRAC 4.5 $\mu\text{m}$	IRAC 5.8 $\mu\text{m}$	IRAC 8.0 $\mu\text{m}$	MIPS 24 $\mu\text{m}$	MIPS 70 $\mu\text{m}$	MIPS 160 $\mu\text{m}$
1.....	0.011	0.018	0.12	0.41	1.86	4.45	2.27
8.....	0.0098	0.015	0.090	0.38	1.94	4.57	2.37
9.....	0.034	0.023	0.14	0.43	1.91	4.52	2.32
11.....	0.0098	0.016	0.10	0.40	1.91	4.55	2.35

ejects PAHs is too slow ( $\tau_{\text{subl}} \gg \tau_{\text{age}} \approx 8 \pm 3$  Myr). Even if PAHs are produced by mechanisms other than sublimation (e.g., shattering of carbonaceous grains), the recondensation of PAHs in the icy mantles of the porous dust component occurs on a timescale of a few thousand years, much shorter than the age of the HR 4796A system:

$$\begin{aligned} \tau_{\text{cond}} &\approx (v_{\text{PAH}} n_d \pi \langle a^2 \rangle)^{-1} \\ &\approx (\pi \langle m_{\text{PAH}} \rangle / 8kT_{\text{gas}})^{1/2} [(2\pi)^{1/2} H / \sigma_p] (\pi \langle a^2 \rangle)^{-1} \\ &\approx 1570 \text{ yr} \ll \tau_{\text{age}}, \end{aligned}$$

where  $T_{\text{gas}}(r) \approx 566(r/\text{AU})^{-1/2}$  K  $\approx 67$  K is the gas temperature,  $\langle m_{\text{PAH}} \rangle \approx 7.99 \times 10^{-22}$  g is the average mass of the PAH molecules with a size distribution like that of the HD 141569A disk (i.e.,  $a_0 = 2.5$  Å and  $\sigma = 0.3$ ; see § 3.2),  $H \approx 0.5$  AU is the vertical scale height (Kenyon et al. 1999),  $\sigma_p \approx 4.90 \times 10^4$  cm $^{-2}$  (Li & Lunine 2003) and  $n_d \approx \sigma_p / (2\pi)^{1/2} H$  are, respectively, the midplane surface density and volume density of the porous dust component at  $r_p = 70$  AU, and  $\pi \langle a^2 \rangle \approx 9.02 \times 10^{-7}$  cm $^2$  (Li & Lunine 2003) is the total grain surface area integrated over the  $dn/da \propto a^{-2.9}$  size distribution, with  $a \in [1 \mu\text{m}, 1 \text{cm}]$  (see Table 1 [model 2] in Li & Lunine 2003). Similarly, the timescale for the accretion of PAHs onto grains at  $r = 203$  AU from the HD 141569A disk is about  $9 \times 10^5$  yr, shorter than the age of the HD 141569A system. Therefore, free-flying PAH molecules are unlikely to exist in the ring regions of the HD 141569A and HR 4796A disks.

To summarize, the respective presence and absence of free-flying PAHs in the HD 141569A and HR 4796A disks can be attributed to the structural differences between these two disks. It is worth noting that the  $\beta$  Pic disk, modeled best as a wedge-shaped disk with a constant opening angle (Artymowicz, Burrows, & Paresce 1989; Backman, Gillett, & Witteborn 1992), is more like the HD 141569A disk than the HR 4796A disk in the sense that the  $\beta$  Pic disk also extends to the inner warm region where the sublimation of icy mantles occurs. However, the existing mid-IR spectra of the  $\beta$  Pic disk do not appear to show any evidence of PAHs (Telesco & Knacke 1991; Knacke et al. 1993; Pantin, Waelkens, & Malfait 1999; Weinberger, Becklin, & Zuckerman 2003). It is not clear whether the absence of PAHs in the  $\beta$  Pic disk is due to its evolutionary status or just because the PAH emission features are swamped by the strong 9.7 and 11.3  $\mu\text{m}$  silicate bands. With an age of  $\approx 12_{-4}^{+8}$  Myr (Barrado y Navascués et al. 1999; Zuckerman et al. 2001), the  $\beta$  Pic disk is more evolved than the HD 141569A disk. *SIRTf* spectroscopy of  $\beta$  Pic at  $\lambda \lesssim 8 \mu\text{m}$  will allow us to draw a more definite conclusion regarding the presence or absence of PAHs in the inner disk of  $\beta$  Pic.

The presence of transiently heated PAH molecules in the dusty environments of Herbig Ae/Be stars has been observationally well established (see, e.g., Whittet et al. 1983; Brooke, Tokunaga, & Strom 1993; Sylvester et al. 1996; Siebenmorgen et al. 2000). Natta & Krügel (1995) have calculated the mid-IR emission spectra expected for PAHs around Herbig Ae/Be stars, assuming a spherical shell geometry for the dust distribution. Sylvester, Skinner, & Barlow (1997) have modeled the SEDs of eight Vega-like dust disks with temperature-fluctuating small silicate and amorphous carbon grains of  $a = 3$  and 5 Å included. So far, however, little has been done in modeling the PAH component in the HD 141569A disk. This work actually represents

the first successful modeling of its entire SED, including the PAH emission features.

#### 4.1. Robustness

The dust model presented here is fully described by 10 parameters: (1)  $a_{\text{min}}^{\text{PAH}}$ ,  $a_0$ ,  $\sigma$ , and  $\phi_{\text{ion}}$  for the PAH component; (2)  $a_{\text{min}}$ ,  $a_{\text{max}}$ ,  $\alpha$ , and  $P$  for the porous dust component; and (3)  $r_{\text{in}}$  and  $r_{\text{out}}$  for the dust spatial distribution  $dn(r)/dr$ . But, as discussed in § 3.1.5, we actually have only three free parameters:  $a_0$ ,  $\sigma$ , and  $\alpha$ .

Other parameters have been constrained by rather general considerations: (1) We take  $a_{\text{min}}^{\text{PAH}} = 3.5$  Å, the radius of the smallest surviving interstellar PAH molecule (§ 3.1.1). (2) We take  $\phi_{\text{ion}} = 1$  since PAHs in the HD 141569A disk are expected to be negatively charged (§ 3.1.4). (3) We take  $a_{\text{min}} = 1 \mu\text{m}$  since this is the smallest size that makes sense in the framework of interstellar dust aggregation (see footnote 5). (4) We take  $a_{\text{max}} = 1$  cm; this size is not well constrained but neither is it crucial, since grains larger than  $\sim 100 \mu\text{m}$  emit like blackbodies and their IR emission spectra are size-insensitive (see Fig. 6). (5) We take  $P = 0.90$  since dust of such a high porosity reproduces the SEDs of the  $\beta$  Pic disk and the HR 4796A disk; a porosity of  $P \approx 0.90$  is expected for fluffy aggregates formed by the accumulation of interstellar dust and is also consistent with the low-density nature of cometary nuclei (§ 3.1.5). (6) We take  $r_{\text{in}}$  to be the radial distance where the refractory dust starts to evaporate (§ 3.1.3). (7) We take  $r_{\text{out}} = 500$  AU, which is expected from disk truncation caused by the tidal effects of HD 141569B (see footnote 8). The dust spatial distribution is taken to be that derived from the near-IR imaging of scattered starlight and mid-IR imaging of dust thermal emission (eq. [13] and § 3.1.3). To be complete, we have also considered models with parameters differing from the nominal ones described above. In the following, except the specifically stated parameters, all other parameters remain the same as those of the canonical cold-coagulation model derived in § 3.2 (model 1; see Fig. 3). See Table 2 for all the key parameters.

1. The  $a_{\text{min}} = 0.1 \mu\text{m}$  model (model 3;  $\alpha = 3.2$ ; Fig. 7, *red solid line*) is almost identical to the  $a_{\text{min}} = 1 \mu\text{m}$  model (model 1; Fig. 3) except for its slight deficiency at the *IRAS* 60  $\mu\text{m}$  band.

2. The  $a_{\text{min}} = 10 \mu\text{m}$  model (model 4;  $\alpha = 3.6$ ; Fig. 7, *blue dotted line*) emits too much in the *IRAS* 60 and 100  $\mu\text{m}$  bands and too little in the Keck II MIRLIN 17.9 and 20.8  $\mu\text{m}$  bands and the *IRAS* 25  $\mu\text{m}$  band.

3. The  $r_{\text{out}} = 1000$  AU model (model 5;  $\alpha = 3.3$ ; Fig. 7, *magenta dashed line*) is almost identical to the  $r_{\text{out}} = 500$  AU model (model 1; Fig. 3) since the cool dust at 500 AU  $< r < 1000$  AU emits very little in the wavelength range of interest here. It emits only  $\sim 10\%$  more at  $\lambda > 200 \mu\text{m}$  than the  $r_{\text{out}} = 500$  AU model.

4. The  $P = 0.95$  model (model 6;  $\alpha = 3.2$ ; Fig. 7, *green long-dashed line*) is almost identical to the  $P = 0.90$  model (model 1;  $\alpha = 3.3$ ; Fig. 3) except for its slight deficiency at the SCUBA 1350  $\mu\text{m}$  band. Its emission at 1350  $\mu\text{m}$  is  $\sim 50\%$  lower than that of the  $P = 0.90$  model.

5. The  $P = 0.80$  model (model 7;  $\alpha = 3.5$ ; Fig. 7, *cyan dot-dashed line*) is almost identical to the  $P = 0.90$  model (model 1;  $\alpha = 3.3$ ; Fig. 3) except that it emits  $\sim 20\%$  less at  $100 \mu\text{m} < \lambda < 600 \mu\text{m}$ .

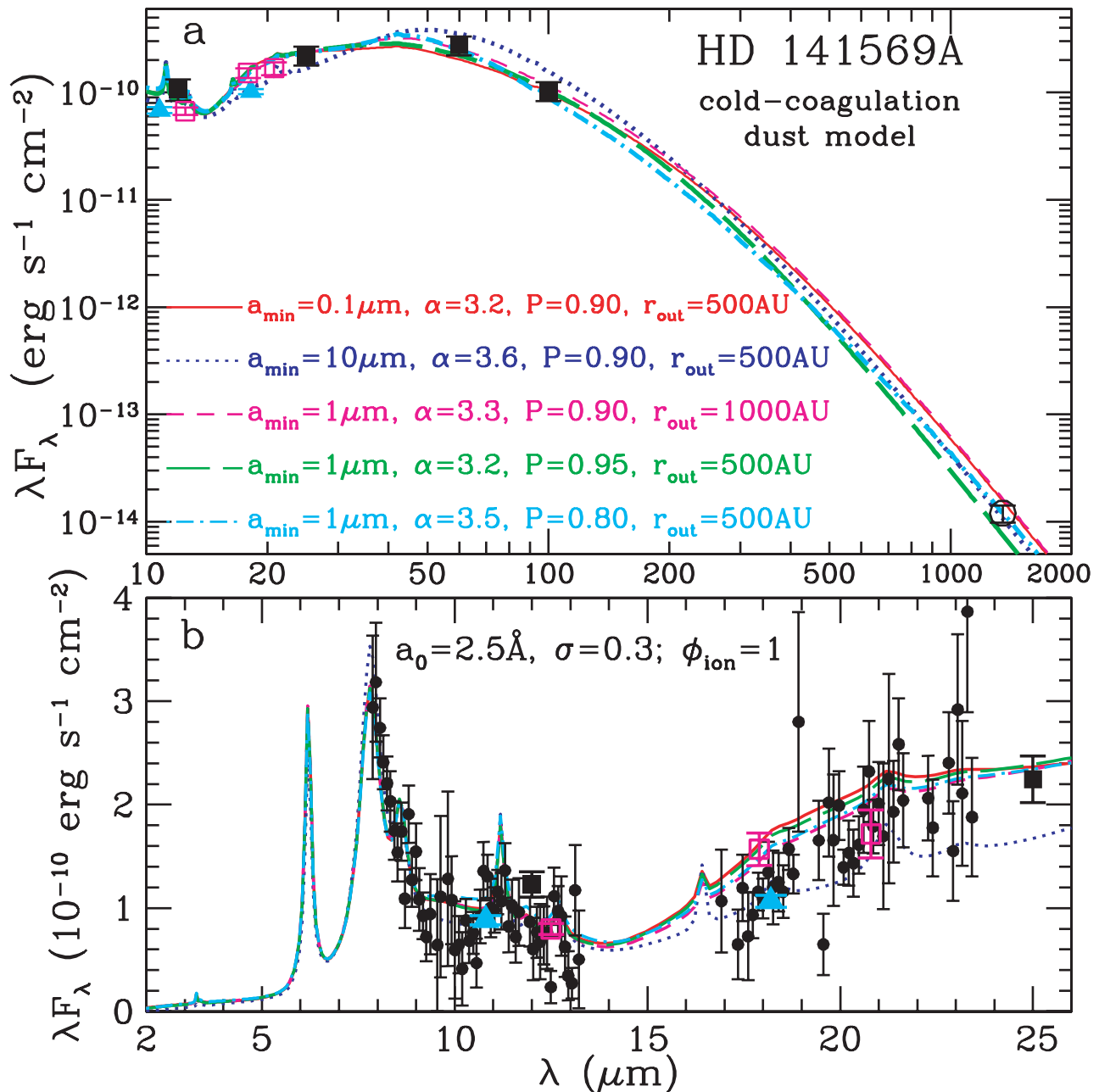


FIG. 7.—Comparison of the observed SED with the theoretical spectra calculated from the cold-coagulation dust models with  $a_{\min} = 0.1\ \mu\text{m}$  (model 3;  $\alpha = 3.2$ ; red solid line),  $a_{\min} = 10\ \mu\text{m}$  (model 4;  $\alpha = 3.6$ ; blue dotted line),  $r_{\text{out}} = 1000\ \text{AU}$  (model 5;  $\alpha = 3.3$ ; magenta dashed line),  $P = 0.95$  (model 6;  $\alpha = 3.2$ ; green long-dashed line), and  $P = 0.80$  (model 7;  $\alpha = 3.5$ ; cyan dot-dashed line). Unless otherwise specified, the remaining parameters of these models (see Table 2) are the same as those of the canonical cold-coagulation model (model 1) described in § 3.2 (see Fig. 3).

In summary, although the canonical cold-coagulation dust model presented in § 3.2 is preferred, some flexibilities are allowed in modeling the HD 141569A SED; i.e., *no fine-tuning is needed* in order for our models to achieve an excellent fit to the observed entire SED. Therefore, the porous dust model made of interstellar materials, previously shown to be successful in reproducing the SEDs of the dust disks around  $\beta$  Pic and HR 4796A, is also robust in modeling the IR emission from the HD 141569A disk.

We have also tried to fit the observed SED using the interstellar PAH size distribution, characterized by  $a_0 = 3.5\ \text{\AA}$  and  $\sigma = 0.4$  (Li & Draine 2001b). As shown in Figure 8a, the model spectrum predicted from the interstellar mixture

of PAH cations (model 8) is also in excellent agreement with the observed mid-IR spectrum. In comparison with the canonical best-fit mixture ( $a_0 = 2.5\ \text{\AA}$  and  $\sigma = 0.3$ ; model 1; see Fig. 3), the interstellar mixture, rich in relatively large PAHs (see Fig. 9), emits a little bit more (less) at wavelengths longward (shortward) of  $\sim 10\ \mu\text{m}$ . This is because large PAHs do not reach temperatures as high as those of small PAHs when heated by energetic photons.

So far, all models assume  $\phi_{\text{ion}} = 1$ . We now consider models containing neutral PAHs. For illustration, two models are considered: a model with a mixture of both neutral and ionized PAHs ( $\phi_{\text{ion}} = 0.5$ ; model 9) and a model only consisting of pure neutral PAHs ( $\phi_{\text{ion}} = 0$ ; model 10).

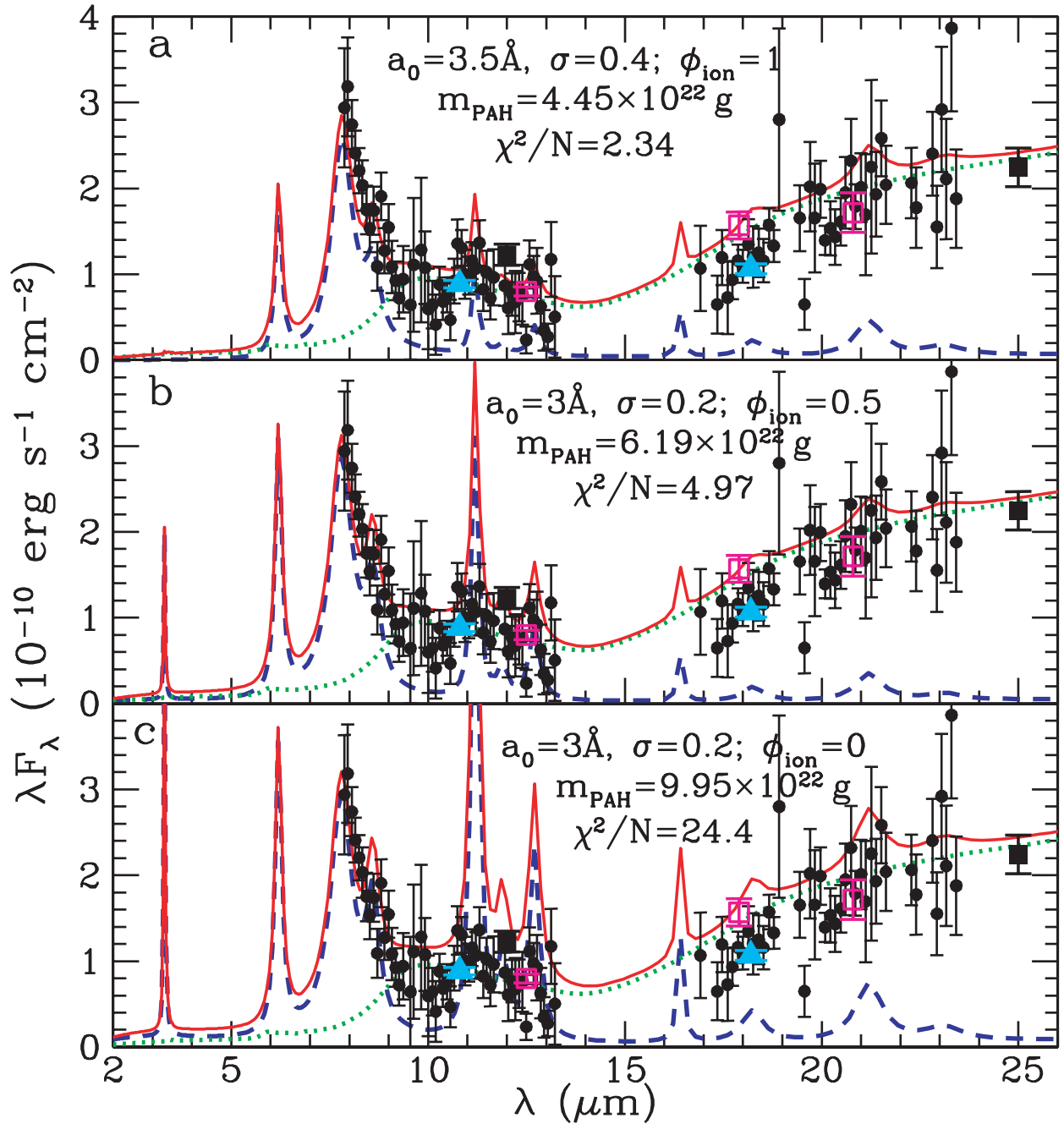


FIG. 8.—Best fits to the CGS3 mid-IR spectrum provided by (a) charged PAHs ( $\phi_{\text{ion}} = 1.0$ ) of interstellar size distribution ( $a_0 = 3.5 \text{ \AA}$  and  $\sigma = 0.4$ ; model 8), (b) a mixture of neutral and charged PAHs ( $\phi_{\text{ion}} = 0.5$ ,  $a_0 = 3.0 \text{ \AA}$ , and  $\sigma = 0.2$ ; model 9), and (c) neutral PAHs ( $\phi_{\text{ion}} = 0$ ,  $a_0 = 3.0 \text{ \AA}$ , and  $\sigma = 0.2$ ; model 10). Other dust parameters (see Table 2) are the same as those of the canonical cold-coagulation model (model 1; Fig. 3).

In Figures 8b and 8c we show, respectively, the best-fit model spectra calculated from the  $\phi_{\text{ion}} = 0.5$  model and from the neutral PAH model. The PAH component of both dust models has a size distribution of  $a_0 \approx 3.0 \text{ \AA}$  and  $\sigma \approx 0.2$  (see Fig. 9). Again, other parameters (see Table 2) are the same as those of the canonical cold-coagulation model (model 1). An inspection of Figure 8c would immediately lead us to rule out the neutral PAH model since this model produces too strong an  $11.3 \mu\text{m}$  feature (as well as a  $12.7 \mu\text{m}$  feature) to reconcile with the CGS3 spectrum of Sylvester et al. (1996). The fit to the CGS3 spectrum by the  $\phi_{\text{ion}} = 0.5$  model is acceptable except that it also appears to

emit a bit too much in the  $11.3 \mu\text{m}$  band, although the quality of the CGS3 spectrum is inadequate to disprove this model. Note that the model-predicted  $11.3 \mu\text{m}$  feature is much sharper than the observed one since we adopt the mean interstellar PAH bandwidths (see Table 7 of Li & Draine 2001b). As a matter of fact, the integrated flux in the calculated  $11.3 \mu\text{m}$  feature is comparable to the observed. The determination of the band strength of the  $11.3 \mu\text{m}$  feature is also complicated by its adjacent continuum. In our dust model, the warm porous dust in the inner region ( $r < 105 \text{ AU}$ ) dominates the continuum underneath the  $11.3 \mu\text{m}$  feature. Future observational studies (e.g., *SIRTF*)

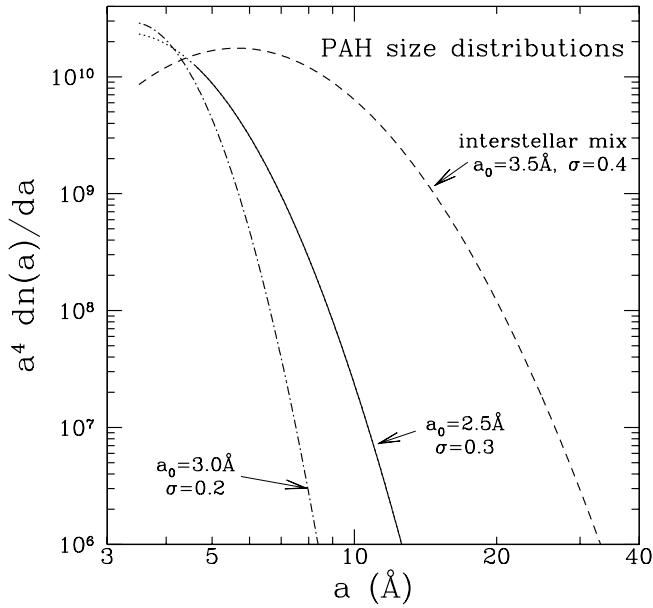


FIG. 9.—Size distributions for the PAH population. A lognormal functional form (see eq. [3]) is assumed. The distribution is determined by a peak parameter  $a_0$  and a width parameter  $\sigma$ :  $a_0 = 2.5 \text{ \AA}$  and  $\sigma = 0.3$  (solid and dotted lines) for the canonical best-fit model (model 1; see Fig. 3 and § 3.2) and  $a_0 = 3.5 \text{ \AA}$  and  $\sigma = 0.4$  (dashed line) for the interstellar PAH model (see Li & Draine 2001b; see Fig. 8a and § 4.1 in this paper);  $a_0 = 3.0 \text{ \AA}$  and  $\sigma = 0.2$  (dot-dashed line) for the  $\phi_{\text{ion}} = 0.5$  and  $\phi_{\text{ion}} = 0$  model (see Figs. 8b and 8c and § 4.1 in this paper). The PAH lower cutoff sizes are all set at  $a_{\text{min}}^{\text{PAH}} = 3.5 \text{ \AA}$  except for one case (dotted line:  $a_{\text{min}}^{\text{PAH}} = 4.6 \text{ \AA}$  [model 11]; see § 4.2 and Fig. 11).

will provide more information on  $\phi_{\text{ion}}$ . But at this moment, it is safe to state that a large fraction of the PAH molecules responsible for the observed mid-IR spectrum in the HD 141569A disk must be ionized.

#### 4.2. PAH Destruction

Upon absorption of an energetic photon, small PAHs, with an insufficient number of internal vibrational modes in which to distribute this photon energy, may be dissociated by ejection of a hydrogen atom, a hydrogen molecule, and/or an acetylene molecule ( $\text{C}_2\text{H}_2$ ). See Appendix A for a detailed discussion of this photoprocess. Following the method described in Appendix A, we have calculated the photodestruction rates ( $k_{\text{des}}$ ) for small PAHs exposed to stellar UV photons in the HD 141569A disk, represented by the photoejection rates of an acetylene molecule. In Figure 10 we show the PAH destruction timescales ( $\tau_{\text{des}} \equiv 1/k_{\text{des}} \propto r^{-2}$ ) for PAHs at  $r = 20, 55,$  and  $90 \text{ AU}$  as a function of PAH size. Apparently, PAHs smaller than  $a \simeq 4.6 \text{ \AA}$  at  $r < 105 \text{ AU}$  are photolytically unstable: they are expected to be photodestroyed in a timescale shorter than the lifetime of the HD 141569A system. Larger PAHs are more stable since they have a larger number of vibrational modes so that they can easily accommodate the absorbed photon energy, and it is therefore less likely for photodissociation to occur.

In order to maintain a stable distribution of small PAHs in the inner region ( $r < 105 \text{ AU}$ ) of the HD 141569A disk, there must exist a source continuously replenishing the

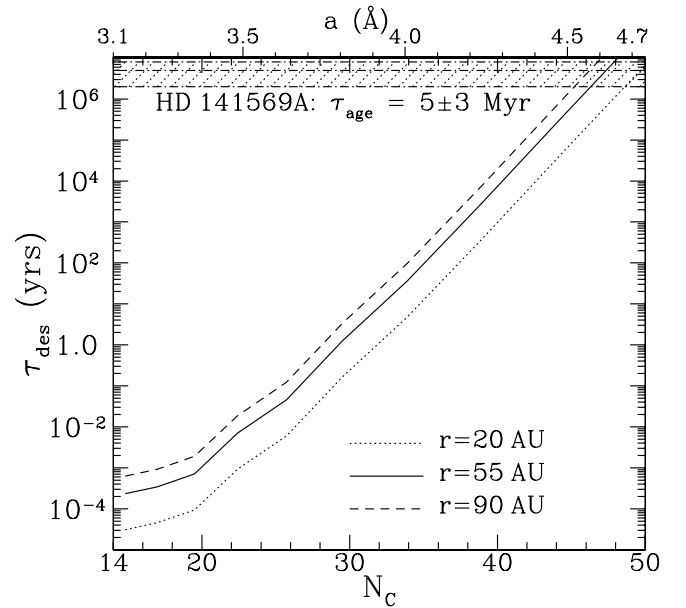


FIG. 10.—Photodestruction timescales for PAHs at  $r = 20, 55,$  and  $90 \text{ AU}$  as a function of size (upper axis) and  $N_C$  (the number of carbon atoms in a PAH molecule; lower axis). Shaded region depicts the age of the HD 141569A system. It is seen that the smallest size of surviving PAHs is  $\sim 4.6 \text{ \AA}$ . But a stable distribution of a population of smaller PAHs is not impossible as long as they are continuously replenished, presumably by sublimation of icy mantles of large grains (in which interstellar PAHs have condensed during the dense molecular cloud phase) produced by collisions of large bodies such as planetesimals and comets.

small PAHs at a rate of

$$\dot{m}_{\text{PAH}} = \int_{r_{\text{in}}}^{105 \text{ AU}} \sigma_{\text{PAH}}(r) 2\pi r dr \times \int_{a_{\text{min}}^{\text{PAH}}}^{\infty} da \frac{dn_{\text{PAH}}}{da} \frac{(4\pi/3)a^3 \rho_{\text{PAH}}}{\tau_{\text{des}}(a, r)}, \quad (17)$$

where the PAH surface density distribution,  $\sigma_{\text{PAH}}(r)$ , is taken to be the same as that of the inner warm porous dust ( $r < 105 \text{ AU}$ ; see § 3.1.3 and eq. [13]):

$$\sigma_{\text{PAH}}(r) = \sigma_{\text{PAH}}^0 \exp \left[ -4 \ln 2 \left( \frac{r/\text{AU} - 55}{70} \right)^2 \right], \quad (18)$$

where  $\sigma_{\text{PAH}}^0$  is the PAH midplane surface density at  $r = 55 \text{ AU}$ . For the canonical cold-coagulation dust model (model 1; § 3.2; Fig. 3) with  $a_0 = 2.5 \text{ \AA}$ ,  $\sigma = 0.3$ ,  $a_{\text{min}}^{\text{PAH}} = 3.5 \text{ \AA}$ , and  $\sigma_{\text{PAH}}^0 \approx 1.17 \times 10^{13} \text{ cm}^{-2}$ , we arrive at  $\dot{m}_{\text{PAH}} \approx 1.11 \times 10^{-3} m_{\oplus} \text{ yr}^{-1}$ ! However, the PAH photodestruction timescales  $\tau_{\text{des}}$  derived above may have been substantially underestimated for two reasons: (1) the photoejection of an acetylene molecule is not equivalent to the complete destruction of a PAH molecule and (2) PAHs can be repaired by accreting carbon atoms and/or ions from the gas (see, e.g., Allain, Leach, & Sedlmayr 1996); the presence of carbon ions in the HD 141569A disk was revealed by the detection of the  $[\text{C II}] 158 \mu\text{m}$  emission (see Lorenzetti et al. 2002). Therefore, it is very likely that the required PAH replenishment rate estimated above has been considerably overestimated. But even if we assume that the above-derived PAH mass-loss rate due to photodestruction is valid and that there is insufficient replenishment implying that there

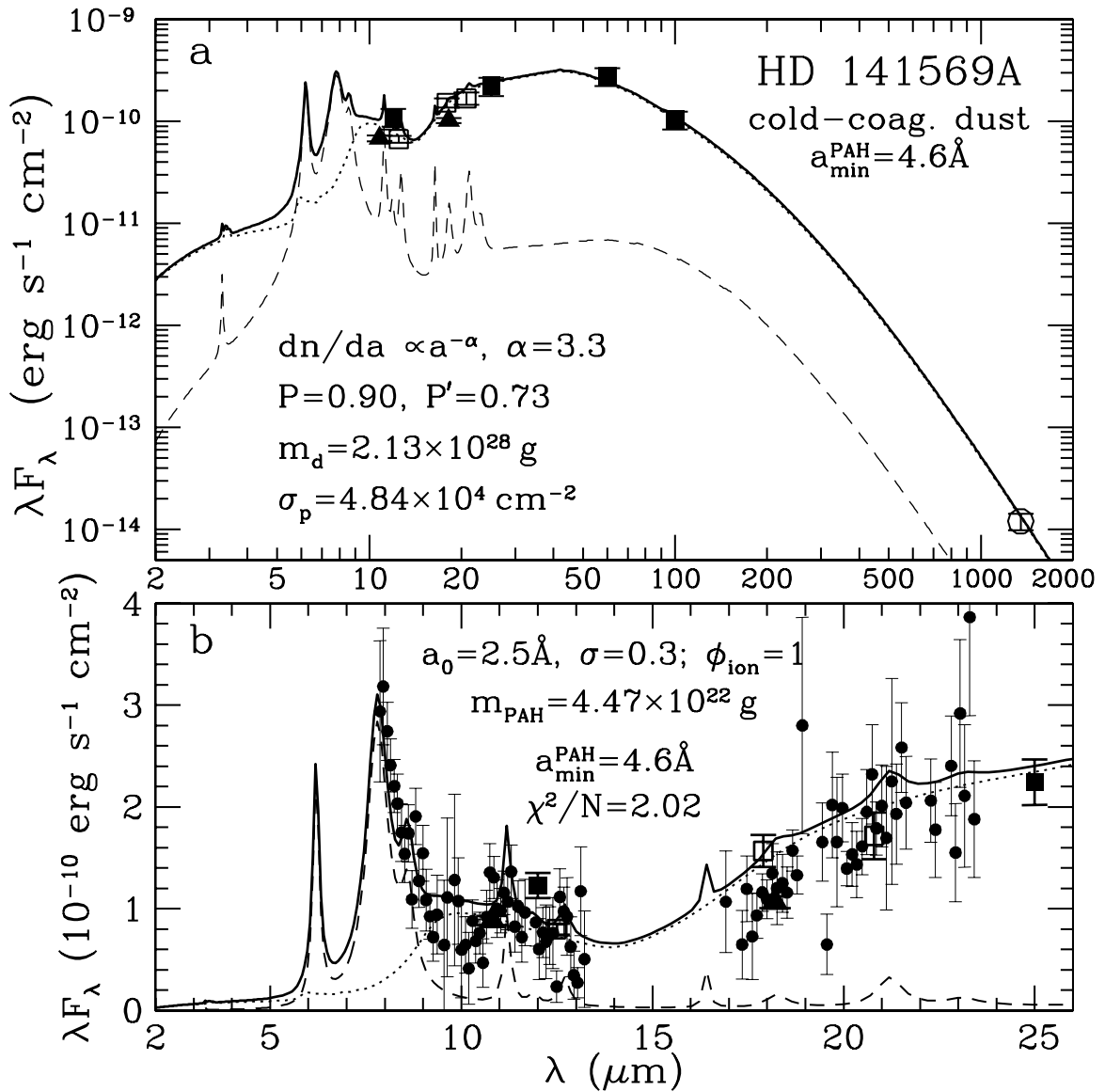


FIG. 11.—Same as Fig. 3 (model 1), except that the PAH component has a larger lower cutoff size  $a_{\min}^{\text{PAH}} = 4.6 \text{ \AA}$  (model 11). In comparison with the canonical cold-coagulation model with  $a_{\min}^{\text{PAH}} = 3.5 \text{ \AA}$  (model 1; see Fig. 3), the  $a_{\min}^{\text{PAH}} = 4.6 \text{ \AA}$  model predicts weaker 3.3 and 6.2  $\mu\text{m}$  features since this model is relatively lacking in small (and hence hot) PAHs (see Fig. 9).

will be no PAHs smaller than  $\sim 4.6 \text{ \AA}$ , our model with  $a_{\min}^{\text{PAH}} = 4.6 \text{ \AA}$  is still able to reproduce the observed SED. This is demonstrated in Figure 11 for the cold-coagulation dust model with  $a_{\min}^{\text{PAH}} = 4.6 \text{ \AA}$  (model 11). Therefore, the exact knowledge of the PAH lower-cutoff size  $a_{\min}^{\text{PAH}}$  is not critical in modeling the HD 141569A SED.

#### 4.3. Radiation Pressure and Poynting-Robertson Drag

In addition to the gravitational attraction from the central star, grains in the HD 141569A disk are subject to (1) radiative outward propulsion as a consequence of momentum transfer from stellar photons and (2) Poynting-Robertson (PR) drag, which causes them to spiral toward the gravitational force center as a consequence of angular momentum loss through radiation (Burns, Lamy, & Soter 1979; Backman & Paresce 1993; Krügel 2003).

The ratio of the radiative force to the gravitational force is

$$\beta_{\text{RP}}(a) = \frac{R_*^2 \int_{912 \text{ \AA}}^{\infty} F_\lambda^* [C_{\text{abs}}(a, \lambda) + (1 - \langle g \rangle) C_{\text{sca}}(a, \lambda)] d\lambda}{4cGM_*(4\pi/3)a^3\rho_{\text{PAH}}}, \quad (19)$$

where  $G$  is the gravitational constant,  $M_*$  ( $\approx 2.3 m_\odot$ ) is the stellar mass,  $C_{\text{sca}}(a, \lambda)$  is the scattering cross section for a grain of size  $a$  at wavelength  $\lambda$ , and  $\langle g \rangle$  (“asymmetry factor”) is the average value of the cosine of the scattering angle.

We have calculated  $\beta_{\text{RP}}$  as a function of dust size for the best-fit canonical cold-coagulation dust model (model 1; see Fig. 3 and § 3.2). As shown in Figure 12a, for grains smaller than  $\sim 10\text{--}20 \mu\text{m}$ , the radiation pressure (RP) overcomes the gravitational attraction (i.e.,  $\beta_{\text{RP}} \gtrsim 1$ ), and, therefore, these grains will be blown out from the HD 141569A disk. But we note that a stable distribution of small grains ( $\lesssim 10\text{--}20 \mu\text{m}$ ) in the disk is possible, provided that they are continuously

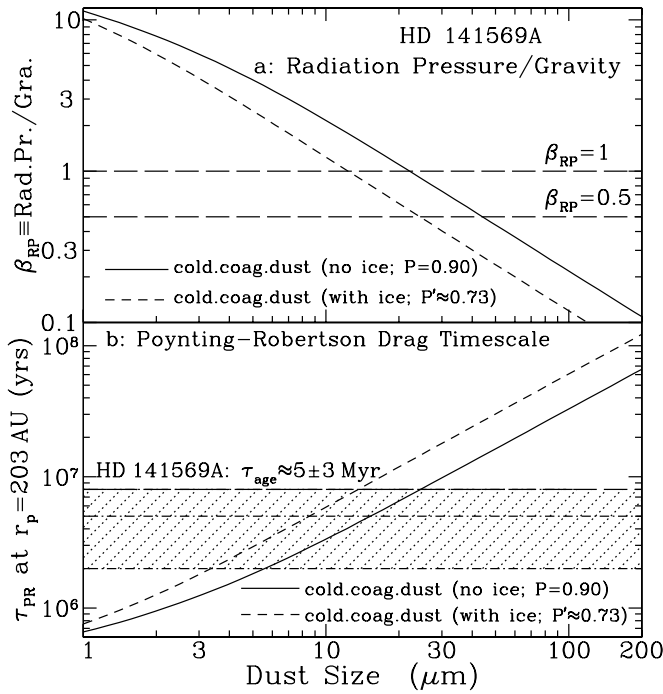


FIG. 12.—(a) Ratio of the radiative repulsion to the gravitational attraction ( $\beta_{\text{RP}}$ ) for the best-fit canonical cold-coagulation dust (model 1; without ice  $P = 0.90$  [solid line] or with ice  $P' = 0.73$  [dashed line]). The long-dashed horizontal lines plot  $\beta_{\text{RP}} = 1$  and  $0.5$  (the smaller value accounting for the fact that particles released at periastron from parent bodies moving on circular orbits only need to have  $\beta_{\text{RP}} = 0.5$  for ejection [Burns et al. 1979], assuming that there is no significant gas drag). (b) Orbit decay timescales  $\tau_{\text{PR}}$  due to the PR drag for the best-fit canonical cold-coagulation dust (model 1; without ice  $P = 0.90$  [solid line] or with ice  $P' = 0.73$  [dashed line]) at a radial distance of  $r_p = 203 \text{ AU}$  from the central star (note  $\tau_{\text{PR}} \propto r^2$ ; see eq. [22]). The shaded region depicts the HD 141569A age ( $\approx 5 \pm 3 \text{ Myr}$ ).

replenished by collisions of larger bodies and/or larger grains so that at any time the disk contains a substantial population of small particles (see Krivov, Mann, & Krivova 2000).

The dust removal rate due to the RP expulsion can be estimated from

$$\dot{m}_{\text{RP}} = \int_{r_{\text{in}}}^{r_{\text{out}}} \sigma(r) 2\pi r dr \int_{a_{\text{min}}}^{10\mu\text{m}} da \frac{dn_{\text{PD}}}{da} \frac{(4\pi/3)a^3 \rho_{\text{PD}}}{\tau_{\text{RP}}(r)}, \quad (20)$$

$$\tau_{\text{RP}}(r) \approx 1900 \left( \frac{r}{203 \text{ AU}} \right)^{3/2} \text{ yr}, \quad (21)$$

where  $\tau_{\text{RP}}$ , the RP timescale, is assumed to be comparable to the local dynamical timescale  $\tau_{\text{dyn}} = 2\pi/\Omega(r)$ , where  $\Omega(r) \equiv (GM_*/r^3)^{1/2}$  is the Keplerian frequency. For the best-fit canonical cold-coagulation model (model 1; see Fig. 3 and § 3.2), the RP dust mass-loss rate is  $\approx 7.87 \times 10^{-6} m_{\oplus} \text{ yr}^{-1}$ .

We have also calculated the PR drag timescale  $\tau_{\text{PR}}(a, r)$  (the time it takes for a grain of size  $a$  at a distance of  $r$  to fall into the central star) from

$$\tau_{\text{PR}}(a, r) = \frac{c^2 r^2 (4\pi/3) a^3 \rho_{\text{PD}}}{R_*^2 \int_{912\text{\AA}}^{\infty} F_{\lambda}^* C_{\text{abs}}(a, \lambda) d\lambda}. \quad (22)$$

In Figure 12b we show that for grains smaller than  $\sim 20 \mu\text{m}$  at a radial distance of  $r_p = 203 \text{ AU}$ , the lifetime associated with the PR drag is shorter than the HD 141569A age, and hence,

these grains will fall into the central star even if they are not ejected by the RP expulsion. For the inner warm dust component at  $r < 105 \text{ AU}$ , grains in the range  $10\text{--}20 \mu\text{m} \lesssim a \lesssim 100\text{--}200 \mu\text{m}$ , although stable against the RP ejection, will be removed from the disk by the PR drag. Since the best-fit cold-coagulation model (model 1) has  $\sim 80\%$  of the total surface areas in grains smaller than  $100 \mu\text{m}$ , these grains must be efficiently replenished by cascade collisions of planetesimals and larger grains. By integrating the PR dust removal rate  $(4\pi/3)a^3 \rho_{\text{PD}} / \tau_{\text{PR}}(a, r)$  over the whole size range and over the entire disk, we estimate the PR dust mass-loss rate to be  $\approx 1.38 \times 10^{-8} m_{\oplus} \text{ yr}^{-1}$  for the best-fit canonical cold-coagulation model (model 1). Therefore, over the life span of HD 141569A, roughly  $39 m_{\oplus}$  of dust is lost by the RP outward expulsion and the PR inward drag.

For the PAH component, the ratio of RP to gravity  $\beta_{\text{RP}} \approx 87.4$  is almost independent of size. This is because PAHs are in the Rayleigh limit at UV/visible wavelengths, where the absorption of stellar photons is such that  $C_{\text{abs}}(a, \lambda) \propto a^3/\lambda$  and  $\langle g \rangle \simeq 0$  (Bohren & Huffman 1983; Krügel 2003). The PR timescale for PAHs at  $r = 55 \text{ AU}$  is about 6000 yr, also independent of size for the same reason. The PAH mass-loss rates due to RP and PR drag are  $\approx 3.09 \times 10^{-8} m_{\oplus} \text{ yr}^{-1}$  and  $\approx 1.95 \times 10^{-9} m_{\oplus} \text{ yr}^{-1}$ , respectively. This implies that a total amount of  $\sim 0.16 m_{\oplus}$  of PAH molecules needs to be replenished over the life span of HD 141569A.

#### 4.4. Predictions for SIRTf

SIRTf will be capable of sensitive imaging using IRAC at 3.6, 4.5, 5.8, and  $8.0 \mu\text{m}$ , and using the MIPS at 24, 70, and  $160 \mu\text{m}$ . In Table 3 we show the band-averaged intensities for our preferred dust models.

SIRTf will also be able to perform low-resolution 5–40  $\mu\text{m}$  and high-resolution 10–37  $\mu\text{m}$  spectroscopic observations using the IRS instrument. IR spectroscopy and imaging will provide powerful constraints on the HD 141569A dust spatial distribution and its chemical composition.

Our best-fit canonical cold-coagulation dust model (model 1; Fig. 3) predicts strong PAH C-C stretching features at 6.6 and  $7.7 \mu\text{m}$ , a weak in-plane C-H bending feature at  $8.6 \mu\text{m}$ , a weak out-of-plane C-H bending feature at  $11.3 \mu\text{m}$ , a very weak C-H stretching feature at  $3.3 \mu\text{m}$ , very weak out-of-plane C-H bending features at 11.9 and  $12.7 \mu\text{m}$ , and very weak C-C bending features at 16.4, 18.3, 21.2, and  $23.1 \mu\text{m}$  (see Li & Draine 2001b for details). With neutral PAHs included (see, e.g., Fig. 8b for the  $\phi_{\text{ion}} = 0.5$  model [model 9], which is not ruled out in the present study), stronger 3.3 and  $11.3 \mu\text{m}$  features are expected. SIRTf spectroscopy at  $\lambda \lesssim 8 \mu\text{m}$  will provide an important test of the PAH model with respect to the PAH size distribution, charging, and survival in the HD 141569A disk.

The cold-coagulation dust model (model 1) produces a broad, smooth, amorphous silicate feature at  $9.7 \mu\text{m}$ , which forms a plateau underneath the  $11.3 \mu\text{m}$  PAH feature (see Fig. 3 and § 3.2). In contrast, the hot-nebula dust model (model 2; see Fig. 4 and § 3.2) predicts two crystalline silicate features at 11.3 and  $23 \mu\text{m}$ . While the  $11.3 \mu\text{m}$  feature is swamped by the PAH C-H out-of-plane bending mode, which is also at  $11.3 \mu\text{m}$ , the  $21 \mu\text{m}$  feature is prominent, and the CGS3 mid-IR spectrum readily places an upper limit of about 10% on crystalline silicate dust (see Fig. 5 and § 3.2). With high-resolution spectroscopy, SIRTf will allow

us to perform more detailed studies of the silicate emission features so as to infer the degree of processing that the HD 141569A dust has experienced.

## 5. CONCLUSION

We have modeled the mid-infrared to submillimeter spectral energy distribution of the double-ring disk around HD 141569A in terms of the porous dust model previously shown to be successful in reproducing the SEDs observed for the disks around  $\beta$  Pic (Li & Greenberg 1998) and HR 4796A (Li & Lunine 2003). The dust is modeled as porous aggregates of either unaltered or heavily processed interstellar materials. While the former (cold-coagulation dust) is made of amorphous silicate dust, carbonaceous dust, H<sub>2</sub>O-dominated ices, and vacuum, the latter (hot-nebula dust) consists of a mixture of crystalline silicates, ices, and vacuum (§ 3.1). For both dust types, a vacuum volume fraction of 90% is assumed (§ 3.1.5). The dust spatial distribution is taken to be that derived from imaging observations of scattered light and dust thermal emission (eq.[13]; § 3.1.3). We take a simple power law for the dust size distribution ( $dn/da \propto a^{-\alpha}$ ) in the size range  $1 \mu\text{m} \lesssim a \lesssim 1 \text{ cm}$ . In addition, a population of PAH molecules with a lognormal size distribution characterized by a peak parameter  $a_0$  and a width parameter  $\sigma$  is invoked to account for the observed 7.7 and 11.3  $\mu\text{m}$  “unidentified infrared” emission features that are generally attributed to PAHs. Our principal results are as follows:

1. The cold-coagulation dust model with a porosity of  $P = 0.90$ , a size distribution power index of  $\alpha \approx 3.3$ , and a total dust mass of  $m_d \approx 3.56 m_\oplus$ , together with a population of charged PAHs with  $a_0 \approx 2.5 \text{ \AA}$ ,  $\sigma \approx 0.3$ , and a total mass of  $m_{\text{PAH}} \approx 7.10 \times 10^{-6} m_\oplus$ , provides an excellent fit to the entire SED, including the PAH mid-IR emission features (§ 3.2; Fig. 3).

2. Although the  $P = 0.90$  hot-nebula dust model provides an overall good fit to the observed SED, it predicts a strong crystalline silicate emission feature at 21  $\mu\text{m}$ , which is not seen in the currently available observational spectrum (§ 3.2; Fig. 4). This places an upper limit of  $\sim 10\%$  on the fraction of hot-nebula dust (i.e., crystalline silicates; § 3.2; Fig. 5).

3. The PAH molecules in the HD 141569A disk are expected to be negatively charged (Fig. 2; § 3.1.4; Appendix

A), assuming that the cosmic-ray ionization of H<sub>2</sub> is the dominant source of electrons (Appendix B). But it has also been shown that models consisting of a mixture of both neutral and charged PAHs are also capable of reproducing the observed PAH IR emission features, provided that the fraction of neutral PAHs is smaller than 50% (Fig. 8; § 4.1).

4. Approximating the photodestruction rate of a PAH molecule by the photoejection rate of an acetylene molecule, PAHs smaller than  $\sim 4.6 \text{ \AA}$  will be photodestroyed in a timescale shorter than the age of the HD 141569A system (Fig. 10; § 4.2; Appendix A). In order to have a stable distribution of small PAHs ( $3.5 \text{ \AA} < a < 4.6 \text{ \AA}$ ) in the HD 141569A disk, we require a continuous replenishment of this component at a rate of  $\sim 1.11 \times 10^{-3} m_\oplus \text{ yr}^{-1}$ . Such a high replenishment rate may not be essential, since (1) the photoejection of a C<sub>2</sub>H<sub>2</sub> molecule does not necessarily lead to the complete destruction of a PAH molecule and (2) the repair of a PAH molecule with a broken C-C bond through reacting with gas-phase C atoms and/ions is ignored in deriving the PAH destruction timescale. Furthermore, we have shown in § 4.2 (Fig. 11) that a model exclusively consisting of PAHs larger than  $\sim 4.6 \text{ \AA}$  also achieves a good fit to the observed SED.

5. Grains smaller than  $\sim 10\text{--}20 \mu\text{m}$  will be radiatively expelled from the disk; grains at  $r = 55 \text{ AU}$  in the size range of  $\sim 10\text{--}20 \mu\text{m} \lesssim a \lesssim 100\text{--}200 \mu\text{m}$  will also be removed from the disk because of the PR inward spiraling drag (at a *closer* [*farther*] distance from the star, *larger* [*smaller*] grains will be removed). Collisions of planetesimals must continuously replenish the dust in the disk at a rate of  $\approx 7.88 \times 10^{-6} m_\oplus \text{ yr}^{-1}$  (§ 4.3). PAHs will also be rapidly removed from the disk by RP and, to a lesser degree, by PR drag. A replenishment rate of  $\approx 3.28 \times 10^{-8} m_\oplus \text{ yr}^{-1}$  is needed to maintain the PAH disk (§ 4.3).

6. Spectroscopic and broadband photometric predictions are made for *SIRTF* observations (§ 4.4).

We thank M. J. Barlow for providing us with the HD 141569A CGS3 mid-IR spectrum. We thank D. E. Backman, A. G. W. Cameron, C. Kulesa, V. La Page, S. Leach, T. W. Rettig, and M. D. Silverstone for helpful discussions, suggestions, and/or clarifications. A. Li thanks the University of Arizona for the Arizona Prize Postdoctoral Fellowship in Theoretical Astrophysics. This research was supported in part by a grant from the NASA origins research and analysis program.

## APPENDIX A

### PHOTOPHYSICS OF POLYCYCLIC AROMATIC HYDROCARBON MOLECULES IN THE HD 141569A DISK

Following the absorption of an energetic photon, a PAH molecule has three major competing decay channels to relax its energy: emission,<sup>14</sup> ionization, and photodissociation. The photodissociation process, critical for small PAHs, has three major loss channels: the loss of a hydrogen atom, a hydrogen molecule, and an acetylene molecule (C<sub>2</sub>H<sub>2</sub>).

We use the Rice, Ramsperger, and Kassel theory (Forst 1973) for the photodissociation rate for a PAH molecule of internal energy  $E$  after excitation:

$$k^X(E) = \begin{cases} \nu_d^X \left(1 - \frac{E_d^X}{E}\right)^{3N-7}, & E > E_d^X, \\ 0, & E \leq E_d^X, \end{cases} \quad (\text{A1})$$

<sup>14</sup> The emission process is dominated by fluorescence (transitions between vibrational states of the same multiplicity) in the IR and partly in the visible. Phosphorescence (transitions between vibrational states of different multiplicity) is less important. In this work we thus only consider IR emission via fluorescence.

TABLE 4  
ACTIVATION ENERGY  $E_d$  AND FREQUENCY FACTOR  $\nu_d$   
(JOCHIMS ET AL. 1994)

Loss Channel X	$E_d^X$ (eV)	$\nu_d^X$ (s <sup>-1</sup> )
H .....	2.8	$1 \times 10^{16}$
H <sub>2</sub> .....	2.9	$1 \times 10^{16}$
C <sub>2</sub> H <sub>2</sub> .....	2.9	$1 \times 10^{15}$

where  $N$  is the number of atoms in the molecule,  $E_d^X$  is the activation energy for the loss of the species X ( $\equiv$ H, H<sub>2</sub>, C<sub>2</sub>H<sub>2</sub>) related to bond dissociation (i.e., the minimum energy required for the dissociation to occur), and  $\nu_d^X$  is the frequency factor for the X-loss channel that reflects the efficiency of intramolecular redistribution of the energy over the vibrational levels of the molecule's ground electronic state after internal conversion. In Table 4 we tabulate the  $E_d$  and  $\nu_d$  parameters for the loss of H, H<sub>2</sub>, and C<sub>2</sub>H<sub>2</sub> experimentally obtained by Jochims et al. (1994) for small PAHs.

The IR photon emission rate for a PAH molecule of internal energy  $E$  is

$$k_{\text{IR}}(E) = \int_{912\text{\AA}}^{\infty} \frac{C_{\text{abs}}^{\text{PAH}}(\lambda) 4\pi B_{\lambda} \{T[E]\}}{hc/\lambda} d\lambda, \quad (\text{A2})$$

where the vibrational temperature  $T$  is obtained from the vibrational energy  $E$  using the Debye model approximation for the PAH enthalpy (see eq. [15] in Li & Draine 2001b).

Assuming that IR emission, ionization, and dissociation are the only relaxation processes for a PAH molecule excited by an energetic photon, the photodestruction rate (approximated by the ejection of an acetylene molecule)  $k_{\text{des}}$  and the dehydrogenation rate  $k_{\text{dhy}}$  for PAHs at a distance of  $r$  from the central star can be obtained from the following equations<sup>15</sup>:

$$k_{\text{des}}(r) = \left(\frac{R_*}{2r}\right)^2 \int_{hc/E_d^{\text{C}_2\text{H}_2}}^{912\text{\AA}} \frac{k_{\text{C}_2\text{H}_2}}{k_{\text{H}} + k_{\text{H}_2} + k_{\text{C}_2\text{H}_2} + k_{\text{IR}}} \frac{C_{\text{abs}}^{\text{PAH}}(\lambda) F_{\lambda}^*}{hc/\lambda} d\lambda, \quad (\text{A3})$$

$$k_{\text{dhy}}(r) = \left(\frac{R_*}{2r}\right)^2 \int_{hc/E_d^{\text{H}}}^{912\text{\AA}} \frac{k_{\text{H}}}{k_{\text{H}} + k_{\text{H}_2} + k_{\text{C}_2\text{H}_2} + k_{\text{IR}}} \frac{C_{\text{abs}}^{\text{PAH}}(\lambda) F_{\lambda}^*}{hc/\lambda} d\lambda. \quad (\text{A4})$$

Following Allain et al. (1996), we adopt an analytical formula for the ionization yield  $Y_{\text{ion}}$  that was based on the experimental data of pyrene and coronene:

$$Y_{\text{ion}} = \begin{cases} 0, & E < E_{\text{IP}}, \\ \frac{0.1(E - E_{\text{IP}})}{8.90 \text{ eV} - E_{\text{IP}}}, & E_{\text{IP}} \leq E < 8.9 \text{ eV}, \\ 0.25 \left(\frac{E}{\text{eV}}\right) - 2.125, & 8.9 \text{ eV} \leq E < 11 \text{ eV}, \\ 0.0596 \left(\frac{E}{\text{eV}}\right) - 0.03, & 11 \text{ eV} \leq E \leq 13.6 \text{ eV} \end{cases} \quad (\text{A5})$$

(Verstraete et al. 1990), where  $E$  and  $E_{\text{IP}}$  (ionization threshold) are in units of eV. We adopt a simple expression for the ionization threshold (see eq. [2] in Weingartner & Draine 2001 for  $Z = 0$ ),

$$\frac{E_{\text{IP}}}{\text{eV}} = 4.4 + \frac{7.19 \text{ \AA}}{a} + \left(\frac{2.94 \text{ \AA}}{a}\right)^2, \quad (\text{A6})$$

where the PAH radius  $a$  is in angstroms. The photoionization rate for a PAH molecule located at a distance of  $r$  from the central star is

$$k_{\text{ion}}(r) = \left(\frac{R_*}{2r}\right)^2 \int_{hc/E_{\text{IP}}}^{912\text{\AA}} \frac{Y_{\text{ion}} C_{\text{abs}}^{\text{PAH}}(\lambda) F_{\lambda}^*}{hc/\lambda} d\lambda. \quad (\text{A7})$$

The electronic recombination rate for a PAH cation is

$$k_{\text{rec}}(r) = \int_0^{\infty} dv_e n_e v_e \pi a^2 \left(1 + \frac{2e\psi}{mv_e^2}\right) 4\pi v_e^2 \left(\frac{m_e}{2\pi k T_{\text{gas}}}\right)^{3/2} \exp\left(-\frac{m_e v_e^2}{2k T_{\text{gas}}}\right) = n_e \left(\frac{8k T_{\text{gas}}}{\pi m_e}\right)^{1/2} \pi a^2 \left(1 + \frac{e^2}{ak T_{\text{gas}}}\right), \quad (\text{A8})$$

where  $n_e$  is the electron density,  $v_e = (8k T_{\text{gas}}/\pi m_e)^{1/2}$  is the electron thermal velocity,  $m_e$  is the electron mass,  $e$  is the electron charge,  $\psi = e/a$  is the PAH electrostatic potential,  $k$  is Boltzmann's constant, and  $T_{\text{gas}}$  is the gas temperature. We take

<sup>15</sup> For simplicity, we assume that the absorbed photon will either ionize the neutral PAH molecule or participate in the photodissociation and vibrational relaxation.

$T_{\text{gas}}(r) = (R_*/2r)^{1/2} T_{\text{eff}} \approx 605(r/\text{AU})^{-1/2}$  K for the HD 141569A disk. In equation (A8) we have assumed that the sticking probability for recombination of an electron on the PAH cation equals 1. The term  $2e\psi/mv_e^2$  accounts for the ‘‘Coulomb focusing’’ effect (Spitzer 1941).

## APPENDIX B

### ELECTRON DENSITY IN THE HD 141569A DISK

Molecular CO gas in the HD 141569A disk has been detected in emission through its rotational transitions at submillimeter wavelengths (Zuckerman et al. 1995) and through its rovibrational transitions at near-IR (Brittain & Rettig 2002; Brittain et al. 2003). Brittain & Rettig (2002) also reported the detection of  $\text{H}_3^+$  emission in the HD 141569A disk. In principle, one can estimate the electron density from the  $\text{H}_3^+$  and CO measurements based on the following assumptions: (1)  $\text{H}_3^+$  is produced mainly through the cosmic-ray (CR) ionization of  $\text{H}_2$  to  $\text{H}_2^+$ ,  $\text{H}_2 + \text{CR} \rightarrow \text{H}_2^+ + e^-$ , followed by the ion-neutral reaction,  $\text{H}_2^+ + \text{H}_2 \rightarrow \text{H}_3^+ + \text{H}$ ; and (2)  $\text{H}_3^+$  is destroyed primarily by its recombination with an electron,  $\text{H}_3^+ + e^- \rightarrow \text{H}_2 + \text{H}$ , and by the ion-neutral reaction with CO,  $\text{H}_3^+ + \text{CO} \rightarrow \text{H}_2\text{CO}^+ + \text{H}$  (McCall et al. 1998). Let  $n_e$ ,  $n_{\text{H}_2}$ ,  $n_{\text{CO}}$ , and  $n_{\text{H}_3^+}$  be the number densities of electrons,  $\text{H}_2$ , CO, and  $\text{H}_3^+$ , respectively; let  $\zeta_{\text{CR}}$  be the cosmic ionization rate; and let  $k_e$  and  $k_{\text{CO}}$  be the rate constants for the  $\text{H}_3^+$  electron recombination and the  $\text{H}_3^+$ -CO reaction, respectively. One can derive the electron density from

$$n_e = \frac{\zeta_{\text{CR}} n_{\text{H}_2} - k_{\text{CO}} n_{\text{CO}} n_{\text{H}_3^+}}{k_e n_{\text{H}_3^+}}. \quad (\text{B1})$$

Brittain & Rettig (2002) estimated the column densities of CO and  $N_{\text{H}_3^+}$  to be  $N_{\text{CO}} \approx 10^{11} \text{ cm}^{-2}$  and  $N_{\text{H}_3^+} \approx 7 \times 10^{10} \text{ cm}^{-2}$  from the CO and  $\text{H}_3^+$  emission spectra obtained for the HD 141569A disk with the NASA Infrared Telescope using the Cryogenic Echelle Spectrograph.<sup>16</sup> With  $\zeta_{\text{CR}} = 3 \times 10^{-17} \text{ s}^{-1}$ ,  $k_{\text{CO}} = 2.0 \times 10^{-9} \text{ cm}^3 \text{ s}^{-1}$ ,  $k_e = 1.8 \times 10^{-7} \text{ cm}^3 \text{ s}^{-1}$  (see McCall et al. 1998 and references therein), and the nominal  $N_{\text{H}_2}/N_{\text{CO}} \approx 10^4$  (Thi et al. 2001), one finds  $n_e < 0$  from equation (B1)! This suggests that CO and  $\text{H}_3^+$  may be distributed in different regions. Brittain & Rettig (2002) suggest that  $\text{H}_3^+$  may originate from the extended envelope of a gas giant protoplanet at  $\sim 7 \text{ AU}$ .

Therefore, it is not appropriate to derive  $n_e$  from the  $\text{H}_3^+$  data; instead, we place an upper limit on  $n_e$  from  $n_{\text{H}_2}$  assuming that the cosmic-ray ionization of  $\text{H}_2$  is the major source of electrons:  $n_e \approx \tau_* \zeta_{\text{CR}} n_{\text{H}_2}$ , where  $\tau_* \approx 5 \text{ Myr}$  is the stellar age.<sup>17</sup> Below we discuss how the number density of molecular hydrogen  $n_{\text{H}_2}$  is obtained.

Assuming that the disk is in vertical hydrostatic equilibrium, the spatial distribution of molecular hydrogen is

$$n_{\text{H}_2}(r, z) = \frac{\sigma_{\text{H}_2}(r)}{\sqrt{2\pi}H(r)} \exp\left[-\frac{1}{2}\left(\frac{z}{H}\right)^2\right], \quad (\text{B2})$$

$$\sigma_{\text{H}_2}(r) = \int_{-\infty}^{+\infty} n_{\text{H}_2}(r, z) dz, \quad (\text{B3})$$

where  $\sigma_{\text{H}_2}$  is the surface density of  $\text{H}_2$ ; the vertical scale height  $H$  is

$$H(r) = \left(\frac{2kT_{\text{gas}}}{GM_*\mu m_{\text{H}}}\right)^{1/2} r^{3/2}, \quad (\text{B4})$$

where  $M_*$  ( $\approx 2.3 m_{\odot}$ ) is the stellar mass,  $m_{\text{H}}$  is the mass of a hydrogen atom, and  $\mu$  is the mean molecular weight ( $\mu \approx 2.34$  for a mixture of  $\text{H}_2$  and He). The total molecular hydrogen mass in the  $r < 130 \text{ AU}$  region around HD 141569A was estimated to be  $m_{\text{H}}^{\text{tot}} \approx 5\text{--}115 m_{\oplus}$  based on the IRAM observations of the  $J = 2\text{--}1$  and  $J = 1\text{--}0$  rotational transitions of CO (Zuckerman et al. 1995).<sup>18</sup> More recently, Brittain & Rettig (2002) found that the CO gas, pumped by strong stellar UV radiation, is confined to the  $17 \text{ AU} < r < 50 \text{ AU}$  region with a total mass of  $\approx 10^{19} \text{ g}$ . Assuming the standard ratio of  $\text{H}_2$  to CO (about  $10^4$ ), this leads to a total  $\text{H}_2$  mass of  $\approx 2 \times 10^{-5} m_{\oplus}$ .

The  $\text{H}_2$  mass inferred by Brittain & Rettig (2002) differs by a factor of  $\approx 7 \times 10^6$  from that of Zuckerman et al. (1995). This is because the UV-pumped CO detected by Brittain & Rettig (2002) only represents material near the star/disk interface and is not indicative of the total gas mass. The UV radiation is quickly scattered by dust and may be influential for only a small annulus of the disk. Submillimeter measurements of CO can measure the cold regions inward of  $\sim 130 \text{ AU}$  (Zuckerman et al. 1995), where most of the cold CO molecules are in the ground vibrational state to which the near-IR observations are not sensitive (Brittain et al. 2003; T. W. Rettig 2003, private communication). Therefore, we will adopt the Zuckerman et al. (1995) results for the  $\text{H}_2$  mass.

<sup>16</sup> This assumes that both CO and  $\text{H}_3^+$  are contained in the  $17 \text{ AU} < r < 50 \text{ AU}$  region around HD 141569A.

<sup>17</sup> Atomic gas has also been seen in the HD 141569A disk. A double-peaked  $\text{H}\alpha$  emission was detected by Andriillat, Jaschek, & Jaschek (1990) and Dunkin et al. (1997), indicating a rotating gas disk close to the star. Dunkin et al. (1997) also detected circumstellar Na I and Ca II absorption lines. Recently, Lorenzetti et al. (2002) reported the detection of  $\text{C}^+$  gas. However, little is known regarding the atomic gas column density and its contribution to the electrons in the disk. Since it is shown in § 3.1.4 that the amount of electrons provided by  $\text{H}_2$  alone is sufficient to (negatively) charge the PAH molecules in the HD 141569A disk, inclusion of electrons from the cosmic-ray ionization of atomic gas would further support our conclusion (i.e., a large fraction of the PAH molecules are [see § 3.1.4 and Fig. 2] and *must be* [see § 4.1 and Fig. 8] charged in the HD 141569A disk). Furthermore, an additional amount of electrons would be provided by the X-ray ionization of  $\text{H}_2$ .

<sup>18</sup> Zuckerman et al. (1995) originally gave  $m_{\text{H}}^{\text{tot}} \approx 20\text{--}460 m_{\oplus}$ . But this was derived from the assumption that the distance from HD 141569A to the Earth is  $d \approx 200 \text{ pc}$ . Adopting  $d \approx 99 \text{ pc}$  (van den Ancker et al. 1998),  $m_{\text{H}_2}$  should be reduced by a factor of  $\approx 4$ .

We assume that in the  $r < 130$  AU region, the spatial distribution of  $H_2$  follows that of the dust (see eq. [13]), i.e.,

$$\sigma_{H_2}(r) = \sigma_{H_2}^p \exp \left[ -4 \ln 2 \left( \frac{r/\text{AU} - 55}{70} \right)^2 \right], \quad r_{\text{in}} < r < 130 \text{ AU}, \quad (\text{B5})$$

where  $\sigma_{H_2}^p$  is the midplane surface density of  $H_2$  at  $r = 55$  AU, which can be derived from  $m_{\text{H}}^{\text{tot}}$  ( $\approx 5\text{--}115m_{\oplus}$ ; Zuckerman et al. 1995):

$$m_{\text{H}}^{\text{tot}} = \int_{r_{\text{in}}}^{130 \text{ AU}} 2m_{\text{H}}\sigma_{H_2}(r)2\pi r dr. \quad (\text{B6})$$

## REFERENCES

- Allain, T., Leach, S., & Sedlmayr, E. 1996, *A&A*, 305, 602  
Allamandola, L. J., Tielens, A. G. G. M., & Barker, J. R. 1985, *ApJ*, 290, L25  
Andrillat, Y., Jaschek, M., & Jaschek, C. 1990, *A&A*, 233, 474  
Artymowicz, P., Burrows, C., & Paresce, F. 1989, *ApJ*, 337, 494  
Artymowicz, P., & Lubow, S. H. 1994, *ApJ*, 421, 651  
Augereau, J. C., Lagrange, A. M., Mouillet, D., & Ménard, F. 1999a, *A&A*, 350, L51  
Augereau, J. C., Lagrange, A. M., Mouillet, D., Papaloizou, J. C. B., & Gorod, P. A. 1999b, *A&A*, 348, 557  
Backman, D. E., Gillett, F. C., & Witteborn, F. C. 1992, *ApJ*, 385, 670  
Backman, D. E., & Paresce, F. 1993, in *Protostars and Planets III*, ed. E. H. Levy & J. I. Lunine (Tucson: Univ. Arizona Press), 1253  
Barrado y Navascués, D., Stauffer, J. R., Hartmann, L., & Balachandran, S. C. 1997, *ApJ*, 475, 313  
Barrado y Navascués, D., Stauffer, J. R., Song, I., & Caillault, J.-P. 1999, *ApJ*, 520, L123  
Bauschlicher, C., & Bakes, E. L. O. 2000, *J. Chem. Phys.*, 262, 285  
Beckwith, S. V. W., Henning, T., & Nakagawa, Y. 2000, in *Protostars and Planets IV*, ed. V. Mannings, A. P. Boss, & S. S. Russell (Tucson: Univ. Arizona Press), 533  
Boccaletti, A., Augereau, J. C., Marchis, F., & Hahn, J. 2003, *ApJ*, 585, 494  
Bohren, C. F., & Huffman, D. R. 1983, *Absorption and Scattering of Light by Small Particles* (New York: Wiley)  
Brittain, S. D., & Rettig, T. W. 2002, *Nature*, 418, 57  
Brittain, S. D., Rettig, T. W., Simon, T., Kulesa, C., DiSanti, M. A., & Dello Russo, N. 2003, *ApJ*, 588, 535  
Brooke, T. Y., Tokunaga, A. T., & Strom, S. E. 1993, *AJ*, 106, 656  
Burns, J. A., Lamy, P. L., & Soter, S. 1979, *Icarus*, 40, 1  
Cameron, A. G. W. 1975, *Icarus*, 24, 128  
———. 1995, *Meteoritics*, 30, 133  
Cameron, A. G. W., & Schneck, P. B. 1965, *Icarus*, 4, 396  
Clampin, M., et al. 2003, *AJ*, 126, 385  
de Grijp, M. H. K., Miley, G. K., & Lub, J. 1987, *A&AS*, 70, 95  
Draine, B. T., & Lee, H. M. 1984, *ApJ*, 285, 89  
Draine, B. T., & Li, A. 2001, *ApJ*, 551, 807  
Dunkin, S. K., Barlow, M. J., & Ryan, S. G. 1997, *MNRAS*, 286, 604  
Fisher, R. S., Telesco, C. M., Piña, R. K., Knacke, R. F., & Wyatt, M. C. 2000, *ApJ*, 532, L141  
Forst, W. 1973, *Theory of Unimolecular Reactions* (New York: Academic)  
Greaves, J. S., et al. 1998, *ApJ*, 506, L133  
Greenberg, J. M. 1968, in *Stars and Stellar Systems*, Vol. VII, ed. B. M. Middlehurst & L. H. Aller (Chicago: Univ. Chicago Press), 221  
Greenberg, J. M., & Li, A. 1999, *Space Sci. Rev.*, 90, 149  
Habing, H. J., et al. 2001, *A&A*, 365, 545  
Henry, T. J., Soderblom, D. R., Donahue, R. A., & Baliunas, S. L. 1996, *AJ*, 111, 439  
Holland, W. S., et al. 1998, *Nature*, 392, 788  
———. 2003, *ApJ*, 582, 1141  
Hudgins, D. M., Bauschlicher, C. W., Allamandola, L. J., & Fetzer, J. C. 2000, *J. Phys. Chem.*, 104, 3655  
Jaschek, M., Jaschek, C., & Egret, D. 1986, *A&A*, 158, 325  
Jayawardhana, R., Fisher, R. S., Hartmann, L., Telesco, C. M., Piña, R. K., & Fazio, G. 1998, *ApJ*, 503, L79  
Jochims, H. W., Rühl, E., Baumgärtel, H., Tobita, S., & Leach, S. 1994, *ApJ*, 420, 307  
Jura, M., Malkan, M., White, R., Telesco, C. M., Piña, R. K., & Fisher, R. S. 1998, *ApJ*, 505, 897  
Kenyon, S. J., Wood, K., Whitney, B. A., & Wolff, M. J. 1999, *ApJ*, 524, L119  
Knacke, R. F., Fajardo-Acosta, S. B., Telesco, C. M., Hackwell, J. A., Lynch, D. K., & Russell, R. W. 1993, *ApJ*, 418, 440  
Koerner, D. W., Ressler, M. E., Werner, M. W., & Backman, D. E. 1998, *ApJ*, 503, L83  
Krivov, A. V., Mann, I., & Krivova, N. A. 2000, *A&A*, 362, 1127  
Krügel, E. 2003, *Physics of Interstellar Dust* (Bristol: Institute of Physics Publishing)  
Kurucz, R. L. 1979, *ApJS*, 40, 1  
Lagrange, A.-M., Backman, D. E., & Artymowicz, P. 2000, in *Protostars and Planets IV*, ed. V. Mannings, A. P. Boss, & S. S. Russell (Tucson: Univ. Arizona Press), 639  
Langhoff, S. R. 1996, *J. Phys. Chem.*, 100, 2819  
Léger, A., & Puget, J. L. 1984, *A&A*, 137, L5  
Li, A., & Draine, B. T. 2001a, *ApJ*, 550, L213  
———. 2001b, *ApJ*, 554, 778  
———. 2002a, *ApJ*, 572, 232  
———. 2002b, *ApJ*, 576, 762  
Li, A., & Greenberg, J. M. 1997, *A&A*, 323, 566  
———. 1998, *A&A*, 331, 291  
Li, A., & Lunine, J. I. 2003, *ApJ*, 590, 368  
Lorenzetti, D., Giannini, T., Nisini, B., Benedettini, M., Elia, D., Campeggio, L., & Strafella, F. 2002, *A&A*, 395, 637  
Malfait, K., Bogaret, E., & Waelkens, C. 1998, *A&A*, 331, 211  
Marsh, K. A., Silverstone, M. D., Becklin, E. E., Koerner, D. W., Werner, M. W., Weinberger, A. J., & Ressler, M. E. 2002, *ApJ*, 573, 425  
Mathis, J. S., Mezger, P. G., & Panagia, N. 1983, *A&A*, 128, 212 (MMP)  
McCall, B. J., Geballe, T. R., Hinkle, K. H., & Oka, T. 1998, *Science*, 279, 1910  
Mouillet, D., Lagrange, A. M., Augereau, J. C., & Ménard, F. 2001, *A&A*, 372, L61  
Natta, A., & Krügel, E. 1995, *A&A*, 302, 849  
Pantín, E., Waelkens, C., & Malfait, K. 1999, in *The Universe as Seen by ISO*, ed. P. Cox & M. F. Kessler (ESA SP-427; Noordwijk: ESA/ESTEC), 385  
Rickman, H. 2003, in *IAU Colloq. 168, Cometary Nuclei in Space and Time*, ed. M. F. A'Hearn (San Francisco: ASP), in press  
Schneider, G., et al. 1999, *ApJ*, 513, L127  
Siebenmorgen, R., Prusti, T., Natta, A., & Müller, T. G. 2000, *A&A*, 361, 258  
Spitzer, L., Jr. 1941, *ApJ*, 93, 369  
Sylvester, R. J., Dunkin, S. J., & Barlow, M. J. 2001, *MNRAS*, 327, 133  
Sylvester, R. J., & Skinner, C. J. 1996, *MNRAS*, 283, 457  
Sylvester, R. J., Skinner, C. J., & Barlow, M. J. 1997, *MNRAS*, 289, 831  
Sylvester, R. J., Skinner, C. J., Barlow, M. J., & Mannings, V. 1996, *MNRAS*, 279, 915  
Szczepanski, J., Wehlburg, C., & Vala, M. 1995, *Chem. Phys. Lett.*, 232, 221  
Takeuchi, T., & Artymowicz, P. 2001, *ApJ*, 557, 990  
Telesco, C. M., & Knacke, R. F. 1991, *ApJ*, 372, L29  
Telesco, C. M., et al. 2000, *ApJ*, 530, 329  
Thi, W. F., et al. 2001, *ApJ*, 561, 1074  
van den Ancker, M. E., de Winter, D., & Tjin A Djie, H. R. E. 1998, *A&A*, 330, 145  
Verstraete, L., Léger, A., d'Hendecourt, L., Defourneau, D., & Dutuit, O. 1990, *A&A*, 237, 436  
Walker, H. J., & Wolstencroft, R. D. 1988, *PASP*, 100, 1509  
Weidenschilling, S. J., & Cuzzi, J. N. 1993, in *Protostars and Planets III*, ed. E. H. Levy & J. I. Lunine (Tucson: Univ. Arizona Press), 1031  
Weinberger, A. J., Becklin, E. E., Schneider, G., Smith, B. A., Lowrance, P. J., Silverstone, M. D., Zuckerman, B., & Terrile, R. J. 1999, *ApJ*, 525, L53  
Weinberger, A. J., Becklin, E. E., & Zuckerman, B. 2003, *ApJ*, 584, L33  
Weinberger, A. J., Rich, R. M., Becklin, E. E., Zuckerman, B., & Matthews, K. 2000, *ApJ*, 544, 937  
Weingartner, J. C., & Draine, B. T. 2001, *ApJS*, 134, 263  
Whipple, F. L. 1999, *Planet. Space Sci.*, 47, 301  
Whittet, D. C. B., Williams, P. M., Zealy, W. J., Bode, M. F., & Davies, J. K. 1983, *A&A*, 123, 301  
Zuckerman, B. 2001, *ARA&A*, 39, 549  
Zuckerman, B., Forveille, T., & Kastner, J. H. 1995, *Nature*, 373, 494  
Zuckerman, B., Song, I., Bessell, M. S., & Webb, R. A. 2001, *ApJ*, 562, L87